The Astrophysical Journal, 691:1109–1127, 2009 February 1 doi:10.1088/0004-637X/691/2/1109

ON THE DYNAMICAL EVOLUTION OF H II REGIONS: AN INVESTIGATION OF THE IONIZED COMPONENT OF W4, A GALACTIC CHIMNEY CANDIDATE. I. KINEMATICS AND DYNAMICS IN THE LATITUDE RANGE $0^\circ \leqslant b \leqslant 3^\circ$

Dominic Lagrois and Gilles Joncas
Département de Physique, de Génie Physique et d'Optique, Centre de Recherche en Astrophysique du Québec, Université Laval, Québec, QC G1K 7P4, Canada;
dominic.lagrois.1@ulaval.ca, joncas@phy.ulaval.ca
Received 2007 December 20; accepted 2008 October 2; published 2009 February 2

ABSTRACT

Fabry-Perot interferometry was used to obtain an Hα survey of the most emissive part of W4, a giant superbubble/H II region located in the Perseus arm. Presented by Normandeau and colleagues as an H I cavity aiming away from the Galactic plane, the void has been morphologically interpreted as a Galactic chimney candidate in interaction with the Galactic corona. We present the kinematical results of nearly five million Hα spectra obtained in the southern portion of the nebula ($0^\circ \leqslant b \leqslant 3^\circ$). Many small-scale radial velocity gradients are detected in the embedded ionized component and are attributed to the photoionization of dense, mostly molecular, fragments found either in or at the periphery of the expanding supershell. The mean local standard of rest radial velocity associated with our Hα survey is found at -42.565 ± 5.204 (1σ) km s^{-1}, redshifted by roughly 5 km s^{-1} from the molecular material found in the vicinity of the large superbubble. Investigation of the Hα line-width measurements has shown W4-south to fall in a transient regime between low velocity dispersions characteristic of small-size Galactic H II regions and supersonic line widths associated with supergiant extragalactic structures. The overall kinematics of W4-south is best explained with the Champagne model for the dynamical evolution of H II regions where at least 10 independent gas flows crisscross the nebula. For the first time, a Champagne flow is seen coming to an end within a nebula, mingling with the surrounding ionized gas. The nature (molecular versus atomic) of the neutral material, prone to erosion, is critical as it leads to much different kinematical interpretations. W4-south appears as a text book example of the last stage in the life of a giant molecular cloud complex.

Key words: Galaxy: halo – ISM: bubbles – ISM: individual (W4) – ISM: kinematics and dynamics – techniques: interferometric

1. INTRODUCTION

Most spiral galaxies are known to be embedded into a hot and ionized gaseous component forming galactic coronae. Introduced by Spitzer (1956) and later confirmed by high-latitude observations (Yentis et al. 1972), this tenuous hot ionized medium (HIM) was also found in a sizeable proportion near the Galactic midplane (Jenkins & Meloy 1974) making the old two-phase interstellar medium (ISM) model proposed by Field et al. (1969) inadequate. Considering the low-latitude X-ray emission, McKee & Ostriker (1977) proposed the now-accepted three-phase ISM model in which the HIM component takes a significant role in the pressure equilibrium.

Highly energetic mechanisms, such as strong stellar winds from massive star clusters and supernova (SN) blast waves, are held responsible for the detection of such a hot plasma at the Galactic plane level. However, the low-latitude constraint associated with these mechanisms forced the scientific community to investigate on different possibilities in order to explain the high-latitude observations. In fact, typical cold corona stars do not have a significant impact, either kinematical or thermal, on the ISM material in their vicinity. Therefore, nonlocal mechanisms were priorized in order to provide energetic feeding able to sustain the ionization of the Galactic corona.

Chevalier & Gardner (1974) presented numerical modelizations of SN remnants in expansion through a stratified Galactic atmosphere where both the particle density and the pressure of the upstream ISM material were meant to exponentially decrease with latitude (Heiles 1991; Dickey & Lockmann 1990). It was found that powerful SNe, located slightly above or under the Galactic midplane, can generate ovoid shells likely to be accelerated through the ISM density gradient. The largest features were seen having their hot embedded material discharged at the corona level. Norman & Ikeuchi (1989) used the expression "Galactic chimneys" to refer to these collimated and highly elongated structures in which energetic photons can easily travel. The authors estimated the number of Galactic chimneys throughout the Milky Way required to explain the high-latitude observations to be a thousand. Unfortunately, Galactic plane surveys (Normandeau et al. 1997; McClure-Griffiths et al. 2001) have not shown the anticipated number of supershells. Even though promising candidates (Müller et al. 1987; Callaway et al. 2000; McClure-Griffiths et al. 2000, 2006) have already been identified in the radio regime, a high-resolution kinematical investigation of the ionized interior of a Galactic chimney candidate yet remains to be accomplished.

Being born mainly in the Galactic plane, H II regions showing large amounts of molecular material, successive generations of massive star clusters through triggering and OB associations are also prime candidates for investigation. Under such conditions, large ovoid H II regions should show ionized gas velocity and density gradients pointing toward the Galactic corona. If such gradients remain undetected, the so-called Champagne phase (Tenorio-Tagle 1979) presents an interesting alternative in order to explain and quantify the dynamical evolution of large H II regions. This model is based on the pressure difference between the freshly photoionized material (at the periphery of dense neutral features exposed to the UV flux of nearby hot stars) and the ambient ISM. Numerical simulations (Bodenheimer et al. 1979; Tenorio-Tagle & Bedjin 1981; Tenorio-Tagle et al. 1982; Franco et al. 1990) predict well-defined linear velocity gradients as the ionized material is carried away from the

pressure discontinuity. Each gradient peaks at an end velocity dependent on the pressure discontinuity (Bodenheimer et al. 1979). For large pressure contrasts ($n_{\rm cloud}/n_{\rm ISM} > 1000$), the end velocity is estimated slightly above 30 km s^{-1} with respect to the eroded feature (this is obtained assuming a speed of sound of roughly 10 km s^{-1} in the ambient ISM). The maximal velocity gradient of the Champagne phase is estimated at 3–5 km s^{-1} pc^{-1} (Bodenheimer et al. 1979). Modelizations have shown larger line widths down the Champagne flow as the ionized material is accelerated away (Cyganowski et al. 2003). This tendency toward line broadening could be partially related to line splitting observed in theoretical Champagne flows (Yorke et al. 1984). Interferometric observations of small-size (2–30 pc) Galactic H II regions (Joncas & Roy 1984; Miville-Deschênes et al. 1995; Godbout et al. 1997; Barriault & Joncas 2007) have shown complicated radial velocity fields in agreement with the Champagne phase. Alternately, the blister model (Hester et al. 1996), mainly governed by the photoionization of photoevaporative flows, was also proposed to explain the evolution of H II regions. The model predicts ionized flows characterized by nonlinear velocity gradients and surprisingly small H II regions that remain relatively close to the boundaries of the associated molecular cloud (Henney et al. 2005). This is explained from the blister model being nonhydrodynamic. For a relatively old H II region showing an ionized extension many times larger than the dimensions covered by the molecular material, the blister model is apparently inadequate (Barriault & Joncas 2007).

We chose to study the kinematical behavior of the giant superbubble/H II region W4, one of the few identified Galactic chimney candidates. Our aims are to (1) determine whether large gas flows are present, (2) quantify the role of stellar winds and UV photons in the photoevaporation of the neutral material, (3) verify if the Champagne phase plays a sizeable role on observed kinematics, (4) investigate if the chimney walls have any kinematical impact, and (5) determine how successive stellar generations have impacted the evolution of the chimney. Our findings suggest that we address this investigation in two sequential papers.

In Section 2, previous work associated with the H II region W4 is presented. Our description mainly focuses on the southern portion of W4 ($0^\circ \leqslant b \leqslant 3^\circ$, hereafter W4-south) while the second paper to follow (Lagrois & Joncas 2009, hereafter Paper II) will investigate the kinematics of the ionized material found at northern latitudes ($3^\circ < b \leqslant 7^\circ$, hereafter W4-north). After a brief description of the data acquisition and reduction techniques in Section 3, in Section 4, we provide the results of our Fabry-Perot Hα survey. Particular areas of the large W4-south region were priorized in order to favor an investigation of the molecular clumps found embedded or at the periphery of the expanding supershell. In Section 5, the time-dynamical evolution of W4-south is discussed through kinematical analysis and interpretation associated with nearly five million Hα spectra. From our kinematical investigation, a spatial scenario of W4-south is proposed in Section 6 while summarized results are presented in Section 7.

2. THE W4 SUPERBUBBLE

Introduced by Westerhout (1958) as an irregular nebula of medium brightness, the H II region W4 is often referred to as the Heart nebula due to the heart-shaped morphology of its southern hemisphere ($0^\circ \leqslant b \leqslant 1^\circ$). It is suggested that outflows from the OB association IC 1805 ($l = 134\overset{\circ}{.}8$, $b = 0\overset{\circ}{.}9$) are responsible for the actual superbubble's expansion (Basu et al. 1999). Proper motion investigation has allowed the identification of 126 stars intrinsic to the star cluster (Shi & Hu 1999). The authors confirmed, through spectroscopic observations, the presence of numerous massive stars; about 40 from spectral types O4 to B2 (including 10 O-type stars) have been identified with a high probability of membership. An important proportion of these massive stars is still found on the main-sequence branch indicating a very young cluster age evaluated at 2.5 Myr (Llorente de Andrés et al. 1982).

UBV photometry, properly corrected for absorption, puts IC 1805 at a heliocentric distance of 2.35 kpc (Massey et al. 1995). Using 8.5 kpc as the distance between the Galactic center and the Sun, we obtained a galactocentric distance of 10.29 kpc for the star cluster. The Canadian Galactic Plane Survey (CGPS) obtained spectroscopic 21 cm line observations across the W3/W4/W5 complex in order to quantify both the emission and the kinematics of the atomic hydrogen (Normandeau et al. 1997). The CGPS-mosaicked data cube covers almost 40 deg^2 on the plane of the sky in the longitude and latitude ranges from 131° to 139° and from −1° to 5°, respectively. The W4 region takes the form of an impressive, elongated H I cavity aiming at the Galactic corona. The void is centered on a radial velocity range between −38.46 and −45.05 km s^{-1} (West et al. 2007) as measured in the local standard of rest (LSR). The large H I supershell was presented as being slightly tilted toward the observer (Normandeau et al. 1996).

Low-latitude ($b \leqslant 1\overset{\circ}{.}5$) far-infrared and radio observations have shown tenuous ionized material beyond the shell boundary that was interpreted as evidences for the percolation of UV photons (Terebey et al. 2003). The authors proposed the southern hemisphere of W4 to lie in a transitional state where particular density-bounded segments can be found on the shell path while the densest emissive clumps seem to energetically confine the H II region.

Dennison et al. (1997) obtained, through narrow-band Hα imaging, a 10° diameter view of the W4 superbubble. The photoionization of the neutral ISM material, compressed by the outer shock wave, induces an emissive Hα counterpart observed on the inner side of the H I supershell. We will, therefore, refer to the W4 supershell as being semineutral, semi-ionized. Considering the apparent dimensions of the superbubble, the authors proposed a timescale formation of roughly 6–10 Myr (about three times the estimated age of the star cluster) and assumed a succession of many star generations in order to have formed the W4 superbubble. Very few Hα features seem to be observed trapped inside the supershell, the ionized mixture being mostly diffuse. Since the compressive outer shock wave is meant to leave very little material behind it (Henny et al. 1999, Chapter 12), we assume the inner diffuse component to be mostly formed of stellar winds and eroded shell/molecular cloud material.

Observations at the James Clerk Maxwell Telescope (JCMT) of the CO (2–1) transition have revealed two elongated cometary clouds, still found embedded in the W4 superbubble, whose remarkable alignment, pointing toward the star cluster IC 1805, provided clues that the UV flux and the mechanical action of stellar winds portrayed the actual shape of the molecular features (Taylor et al. 1999). Based on well-detected radial velocity gradients, the authors proposed spatial scenarios where, in the first case, the southern fragment G134.9+1.4 is located behind the star cluster moving away toward the rear side of

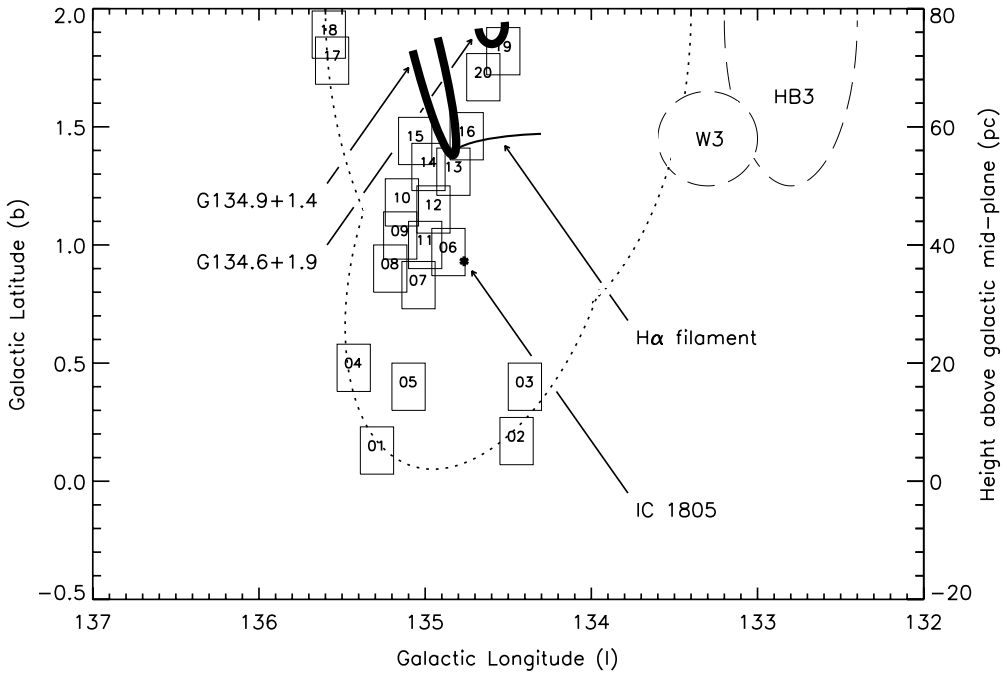

Figure 1. Schematic diagram of W4-south. The numbers coincide with the optical centers of the 20 gathered Hα fields. Boxes enclosed the area covered by each field. The dotted line is related to the semineutral, semi-ionized W4 supershell while thick solid lines and the regular bold line are associated, respectively, with the CO (2–1) transition emission of the two embedded (large) molecular fragments and the thin Hα filament. Also included are the H II region W3 and the SN remnant HB3 (long-dashed lines).

the superbubble. Dennison et al. (1997) particularly noticed a bright Hα filament roughly 0.°5 above the star cluster and extending from the western side of G134.9+1.4. The authors interpreted the filament as the anticipated ionized component resulting from the interaction between the cloud fragment and the UV flux of the star cluster. Secondly, the overall kinematics of G134.9+1.4 and the northern cloud fragment, G134.6+1.9, are said to be roughly similar if, inversely, the latter one is located in front of the star cluster. The reader is referred to Figure 1, presenting a schematic view of W4-south, in order to visualize the location of the different structures. The smaller H II region W3 and the SN remnant HB3 were added to the W4 superbubble, as shown in Figure 1. Aside from the two cometary clouds, observations of the CO (1–0) transition have also provided evidences of numerous molecular fragments still found in the W3/W4/W5 star-forming complex (Heyer et al. 1998). A contour plot extracted from the Five College Radio Astronomy Observatory (FCRAO) CO (1–0) survey of the second Galactic quadrant is added to the large-scale view of the Hα emission in W4-south, as shown in Figure 2. Compressed clumps of molecular material can be seen at the periphery of the expanding southern supershell. Thin fragments, confined inside the shell, are also detected east of the star cluster. The contours are traced out between 5 and 40 K km s^{-1} with a spacing of 5 K km s^{-1}.

In order to estimate the kinematical impact attributed to the photoionization of these neutral structures and their role played on the dynamical evolution of the H II region, an Hα survey via Fabry-Perot interferometry was carried out on the embedded ionized component found in W4-south.

3. OBSERVATIONS AND DATA REDUCTION

Hα observations were performed between 2003 and 2007 using the Ritchey–Chrétien 1.6 m telescope of the Observatoire du mont Mégantic (OmM). The data were gathered using the Fabry-Perot of New Technology for the Observatoire du mont Mégantic (FaNTOmM) device system composed of a $f/2$ focal reducer, a Fabry-Perot Interferometer (FPI), and an Image Photon Counting System (IPCS). Both the parallelism and the spacing between the plates of the FPI were monitored using a servo-control system. The finesse varied slightly between observing runs giving spectral resolutions between 0.15 and 0.21 Å/channel. The central interference order of the FPI was fixed at $m_0 = 765$ for a free spectral range of 8.56 Å centered on the Hα rest frequency. The spectral scanning covers seven interference orders (labeled m_0, $m_{\pm1}$, $m_{\pm2}$, $m_{\pm3}$) for a total range of 60 Å (roughly seven times the free spectral range). Calibration interferograms were obtained using the λ6598.95 Å Ne line. To isolate the Hα emission from other ionic lines, narrow-band ($\Delta\lambda_{\rm FWHM} = 10$ Å) interference filters, slightly redshifted from λ6562.78 Å in order to compensate for blueshifting effects caused by cold ambient temperatures, were used. Emission attributed to the peripheral scanned orders ($m_{\pm2}$, $m_{\pm3}$) is, therefore, flattened out by the narrow transmissive bands.

The use of the Panoramix $f/2$ focal reducer (Godbout et al. 1998) allowed a 12.′3 × 12.′3 field of view (FOV) for a spatial resolution of 1.″45/pixel. The IPCS camera (Hernandez et al. 2003) is composed of a Gallium–Arsenide (GaAs) photocathode, a high-voltage intensifier tube, and a regular 1024 × 1024 CCD. Instead of using the 1024 × 1024 40 frames per second mode of the CCD, we used the hard binned mode of 512 × 512 at 80 frames per second. This type of camera differs from other IPCS systems due to the centering work of events done in real time using the ADHOCw[1] software as opposed to a usual hardwiring system. This method allows for very small readout times. Therefore, each channel can be observed numerous times and summed at the end of the acquisition in order to increase

[1] http://www-obs.cnrs-mrs.fr/adhoc/adhoc.html

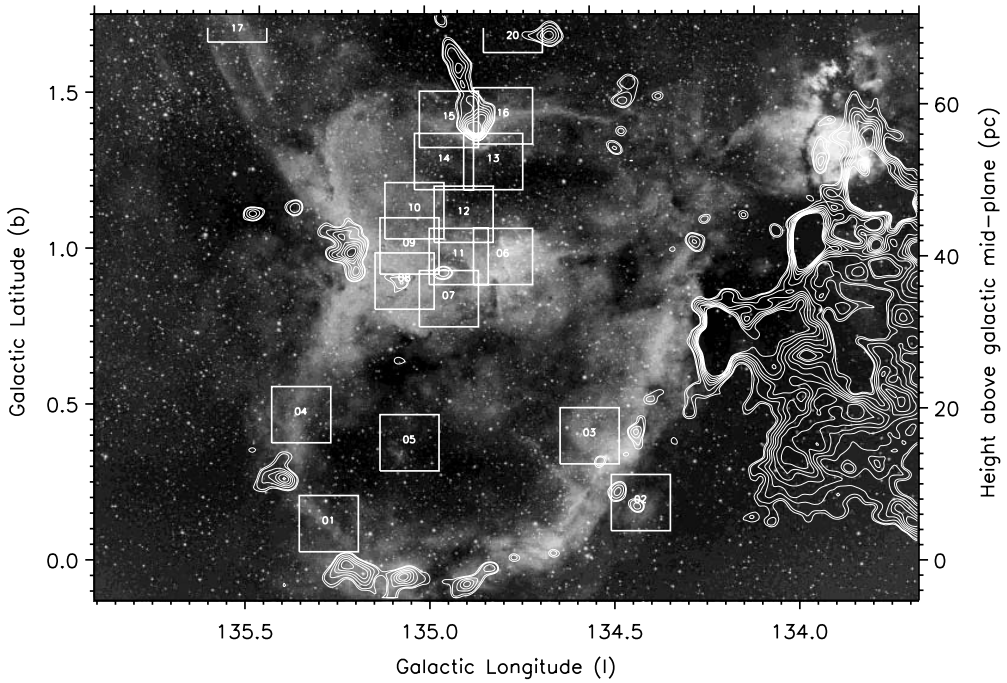

Figure 2. Narrow-band imaging of the Hα emission across W4-south. Courtesy of astro-imager Richard Crisp, the image was taken on 2004 August 27–28, from Castro Valley, CA, USA. A custom 50 mm narrow-band emission line filter was used centered on λ6563.0 Å. The filter had a 30 Å FWHM transmissive band. A 2 hr exposure time was required. A contour plot of the CO (1–0) transition emission in the vicinity of W4-south is added to the Hα image. An integrated intensity map of the molecular emission was extracted from the FCRAO CO (1–0) observations. The spectral collapse of the data cube was made for LSR radial velocities between -22.90 and -63.30 km s^{-1}. Eight contour levels are drawn between 5 and 40 K km s^{-1}. As in Figure 1, numbers coincide approximately with the location of the Fabry-Perot observations.

the signal-to-noise ratio (S/N; Gach et al. 2002). Combined with the no-readout noise characteristic of IPCS cameras, the FaNTOmM system represents an ideal device to study particularly faint astronomical objects. Exposure times varied according to the particular Hα emission of individual fields. The bright emission associated with targeted regions in the direct vicinity of the star cluster IC 1805 allowed us to obtain reliable kinematical information in approximately 120 minutes. However, farther fields undergoing emission attenuation through flux dilution or due to a simple lack of ionized material required a more important number of cycles in order to obtain acceptable S/Ns. Roughly, 4–5 hr were needed for the faintest fields of our Hα survey of W4-south.

Data reduction was carried out using IDL routines (Daigle et al. 2006), specially tailored to reproduce the method used for the TAURUS FP spectrometer (Atherton et al. 1982). For each field, computation of the phase map and its application to the observed interferogram allowed us to obtain a three-dimensional (l, b, λ) raw data cube. Sky subtraction has been found to be highly complicated since the dimensions of the superbubble are much larger than those of a single FOV; night-sky emission was, therefore, not available near the fields' edges, a method typically used for extragalactic observations. In order to subtract from Hα profiles contaminant night-sky lines found in the scanned wavelength interval (Osterbrock et al. 1996), a multi-component Gaussian fit giving the amplitude, spectral position (or radial velocity), and observed line width of each component was applied to each emission spectrum. The minimal S/N allowed for a fitted line was fixed at 3. All radial velocities were measured with respect to the LSR using the optical convention. For close objects like W4, the two conventions, radio or optical, show a difference in radial velocities of the order of a fraction of km s^{-1}, below the typical uncertainty of our velocity measurements (see Section 4).

In order to extract purely kinematical information from Hα line widths, we supposed each contribution to the observed broadening to be approximated by independent Gaussian profiles. Individual widths related to the instrumental and thermal profiles, and the Hα-fine structure, were therefore quadratically subtracted from each observed line width. The latter is discussed by Dyson & Meaburn (1971) with a contribution of 1.37 km s^{-1}. Thermal broadening was obtained for an electronic temperature of 7400 K using the galactocentric electronic temperature gradient for known H II regions (Paladini et al. 2004). Finally, the instrumental contribution was taken as the width of the Ne-line calibration profile, also properly corrected for thermal broadening intrinsic to excited neon plasmas (Sáinz et al. 2005). The corrected Hα line widths provide the kinematical broadening attributed to turbulence and radial velocity gradients along the line of sight (LOS).

4. KINEMATICAL RESULTS

Bounded boxes, in Figures 1 and 2, indicate the location of the FPI observations and the area covered by each field. A total of 20 fields were obtained in order to estimate the kinematical impact of neutral structures (H I walls, molecular clouds embedded inside the supershell or found partially compressed near the outer shock wave) on the ionized gas's overall behavior. The northern boundary of the Hα image used in Figure 2 is fixed at $b = 1\overset{\circ}{.}75$ and, therefore, does not allow to indicate the location of Fields 17–19 (see Section 4.2). Due to particularly faint Hα emission found for Fields 05, 19, and 20, we performed a 2×2 spatial binning of each data cube. The remaining fields were kept at their original spatial resolution. A Gaussian kernel with FWHM = 2 pixels has been used as a spatial smoothing filter in order to emphasize structures in the velocity maps.

For each field, Tables 1 and 2, respectively, present the main results obtained from individual radial velocity and corrected

Table 1
LSR Radial Velocity Investigation

Field	Optical Center (l, b)	$\langle v_{i,\mathrm{LSR}} \rangle$ (km s^{-1})	$\sigma_{v_{i,\mathrm{LSR}}}$ (km s^{-1})	Skewness	Kurtosis Excess	Location
01	(135.°29, 0.°10)	-45.340 ± 0.008	4.017 ± 0.006	0.17	1.06	Southern hemisphere
02	(134.°45, 0.°17)	-43.290 ± 0.009	4.274 ± 0.006	0.63	2.05	Southern hemisphere
03	(134.°62, 0.°40)	-42.895 ± 0.008	4.144 ± 0.006	−0.07	2.21	Southern hemisphere
04	(135.°45, 0.°48)	-42.480 ± 0.009	4.317 ± 0.006	−0.19	3.23	Southern hemisphere
05	(135.°10, 0.°40)	-40.790 ± 0.022	5.529 ± 0.016	−0.55	1.05	Southern hemisphere
06	(134.°81, 0.°95)	-40.781 ± 0.012	5.986 ± 0.008	−0.08	0.32	IC 1805 vicinity
07	(134.°97, 0.°83)	-46.111 ± 0.011	5.343 ± 0.007	0.19	0.69	IC 1805 vicinity
08	(135.°13, 0.°90)	-40.307 ± 0.009	4.798 ± 0.007	0.34	0.49	IC 1805 vicinity
09	(135.°10, 1.°04)	-46.607 ± 0.007	3.754 ± 0.005	0.67	1.31	IC 1805 vicinity
10	(135.°08, 1.°13)	-44.436 ± 0.007	3.589 ± 0.005	0.25	0.70	IC 1805 vicinity
11	(134.°96, 0.°95)	-41.075 ± 0.008	4.029 ± 0.006	−0.08	3.33	IC 1805 vicinity
12	(134.°93, 1.°11)	-40.004 ± 0.009	4.596 ± 0.006	0.26	0.72	IC 1805 vicinity
13	(134.°82, 1.°26)	-45.144 ± 0.009	4.669 ± 0.007	0.48	1.21	G134.9+1.4 fragment
14	(134.°98, 1.°30)	-42.955 ± 0.009	4.403 ± 0.006	−0.09	0.15	G134.9+1.4 fragment
15	(134.°96, 1.°36)	-39.251 ± 0.011	4.094 ± 0.008	0.29	0.57	G134.9+1.4 fragment
16	(134.°80, 1.°40)	-40.789 ± 0.008	4.046 ± 0.006	0.70	1.26	G134.9+1.4 fragment
17	(135.°52, 1.°78)	-40.888 ± 0.009	4.661 ± 0.007	0.17	0.88	W4 eastern wall
18	(135.°65, 1.°89)	-44.751 ± 0.009	4.407 ± 0.006	0.35	0.50	W4 eastern wall
19	(134.°53, 1.°82)	-36.699 ± 0.017	4.185 ± 0.012	0.17	1.24	G134.6+1.9 fragment
20	(134.°72, 1.°69)	-37.202 ± 0.025	6.379 ± 0.018	0.33	0.74	G134.6+1.9 fragment

Table 2
Line-Width Investigation

Field	Optical Center (l, b)	$\langle \beta_{i,\mathrm{corr}} \rangle$ (km s^{-1})	$\sigma_{\beta_{i,\mathrm{corr}}}$ (km s^{-1})	Skewness	Kurtosis Excess	Location
01	(135.°29, 0.°10)	8.338 ± 0.007	3.728 ± 0.005	0.03	−0.35	Southern hemisphere
02	(134.°45, 0.°17)	9.062 ± 0.011	5.339 ± 0.007	1.49	2.50	Southern hemisphere
03	(134.°62, 0.°40)	9.761 ± 0.006	2.978 ± 0.004	0.26	2.39	Southern hemisphere
04	(135.°45, 0.°48)	10.933 ± 0.007	3.741 ± 0.005	0.78	1.27	Southern hemisphere
05	(135.°10, 0.°40)	10.972 ± 0.022	5.564 ± 0.016	0.37	−0.35	Southern hemisphere
06	(134.°81, 0.°95)	10.233 ± 0.006	3.032 ± 0.004	0.54	0.92	IC 1805 vicinity
07	(134.°97, 0.°83)	9.493 ± 0.008	3.978 ± 0.006	0.38	−0.35	IC 1805 vicinity
08	(135.°13, 0.°90)	9.535 ± 0.006	2.958 ± 0.004	0.19	0.28	IC 1805 vicinity
09	(135.°10, 1.°04)	7.412 ± 0.004	1.918 ± 0.003	−0.28	0.42	IC 1805 vicinity
10	(135.°08, 1.°13)	8.080 ± 0.003	1.688 ± 0.002	0.01	0.54	IC 1805 vicinity
11	(134.°96, 0.°95)	5.795 ± 0.004	2.224 ± 0.003	−0.03	−0.06	IC 1805 vicinity
12	(134.°93, 1.°11)	8.925 ± 0.004	2.317 ± 0.003	0.10	0.07	IC 1805 vicinity
13	(134.°82, 1.°26)	11.473 ± 0.007	3.420 ± 0.005	0.20	0.28	G134.9+1.4 fragment
14	(134.°98, 1.°30)	10.803 ± 0.005	2.744 ± 0.004	−0.22	0.20	G134.9+1.4 fragment
15	(134.°96, 1.°36)	9.792 ± 0.008	4.047 ± 0.006	0.08	−0.05	G134.9+1.4 fragment
16	(134.°80, 1.°40)	9.328 ± 0.007	3.727 ± 0.005	0.64	1.07	G134.9+1.4 fragment
17	(135.°52, 1.°78)	5.620 ± 0.005	2.323 ± 0.003	0.45	0.95	W4 eastern wall
18	(135.°65, 1.°89)	5.918 ± 0.006	2.991 ± 0.004	0.47	0.34	W4 eastern wall
19	(134.°53, 1.°82)	10.622 ± 0.018	4.449 ± 0.012	0.41	0.42	G134.6+1.9 fragment
20	(134.°72, 1.°69)	12.245 ± 0.017	4.251 ± 0.012	0.02	−0.12	G134.6+1.9 fragment

line-width distributions; mean values ($\langle v_{i,\mathrm{LSR}} \rangle$ and $\langle \beta_{i,\mathrm{corr}} \rangle$) are presented in Column 3 while standard deviations ($\sigma_{v_{i,\mathrm{LSR}}}$ and $\sigma_{\beta_{i,\mathrm{corr}}}$) for each distribution are shown in Column 4. Skewness and kurtosis excess are also, respectively, given in Columns 5 and 6. A brief comment related to the location of each field is proposed in Column 7. From now on, the label "i" will be referred to the field's number (e.g., $\langle v_{01,\mathrm{LSR}} \rangle$ corresponds to the mean radial velocity observed in Field 01). In Tables 1 and 2, uncertainties on mean values and one standard deviations correspond to statistical uncertainties (inversely proportional to $\sqrt{N}$, where N is the number of events in each distribution). Kinematical uncertainties, for each radial velocity and corrected line-width point, were also calculated with the method proposed by Lenz & Ayres (1992). For each field, histograms of the kinematical uncertainties have mainly shown Poissonian characteristics. Table 3 presents the mean uncertainties extracted from the different distributions.

The FPI observations were carried out to investigate five different portions of W4-south: the southern hemisphere (Fields 01–05), the star cluster vicinity (Fields 06–12), the molecular cloud fragment G134.9+1.4 (Fields 12–16), the W4-eastern wall at intermediate latitudes (Fields 17 and 18), and the molecular cloud fragment G134.6+1.9 (Fields 19 and 20). Sections 4 and 5 will be divided into four subsections: (1) a general overview using the kinematical information obtained from our Hα survey taken as a whole followed by localized investigations

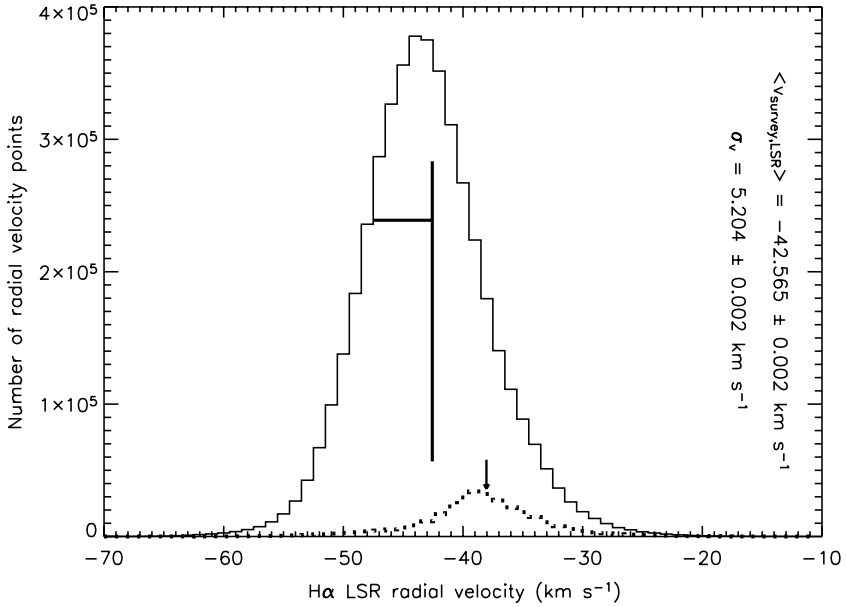

Figure 3. Hα LSR radial velocity distribution of W4-south. Both the mean LSR radial velocity and the statistical one standard deviation, found, respectively, at -42.565 ± 0.002 km s^{-1} and 5.204 ± 0.002 km s^{-1}, are schematically represented by the vertical and horizontal thick solid lines. A slight asymmetry is found with a skewness being estimated at 0.29. The kurtosis excess is found at 0.87. A normal distribution would give a skewness and a kurtosis excess of 0. The dotted histogram corresponds to the LSR radial velocity distribution of the interflow medium of W4-south. The mean of the distribution, estimated at -38.04 ± 0.01 km s^{-1}, is indicated by the solid arrow.

Table 3
Mean Kinematical Uncertainties on LSR Radial Velocity and Line-Width Measurements

Field	$\langle e_{i,\lambda} \rangle$ (km s^{-1})	$\langle e_{i,\beta} \rangle$ (km s^{-1})
01	0.498 ± 0.001	1.512 ± 0.088
02	0.644 ± 0.001	1.993 ± 0.154
03	0.669 ± 0.002	1.640 ± 0.239
04	0.599 ± 0.001	0.898 ± 0.004
05	0.855 ± 0.003	2.254 ± 0.054
06	0.470 ± 0.001	0.616 ± 0.079
07	0.574 ± 0.002	0.997 ± 0.040
08	0.468 ± 0.001	0.701 ± 0.071
09	0.376 ± 0.001	0.598 ± 0.050
10	0.399 ± 0.001	0.524 ± 0.003
11	0.388 ± 0.001	1.018 ± 0.066
12	0.517 ± 0.002	0.609 ± 0.003
13	0.497 ± 0.001	0.718 ± 0.004
14	0.545 ± 0.001	0.852 ± 0.015
15	0.530 ± 0.001	0.727 ± 0.004
16	0.602 ± 0.001	0.933 ± 0.045
17	0.571 ± 0.002	1.310 ± 0.004
18	0.566 ± 0.001	2.916 ± 0.106
19	1.220 ± 0.003	2.897 ± 0.085
20	0.690 ± 0.002	1.361 ± 0.007

of the ionized gas's kinematical behavior in the vicinity of (2) molecular and (3) atomic material. A last subsection will be added to discuss the (4) interflow medium of W4-south.

4.1. General Overview

Nearly five million Hα spectra were obtained for Fields 01–20. Combined together, distributions for the LSR radial velocities and corrected Hα line widths are, respectively, presented in Figures 3 and 4. The mean LSR radial velocity is found at $\langle v_{\rm survey,LSR} \rangle = -42.565 \pm 0.002$ km s^{-1}, in agreement with the LSR radial velocity range revealing the H I cavity in the radio regime (see Section 2). The standard deviation of the radial velocity distribution is found at $\sigma_v = 5.204 \pm 0.002$ km s^{-1}. The asymmetry coefficient is found at 0.29, an indication for an overabundance of radial velocity points above -35 km s^{-1}. This contributes for a mean radial velocity slightly redshifted from the most probable value of the distribution near -44 km s^{-1}. The distribution has a kurtosis excess of 0.87. Since a perfect Gaussian would show a value of 0, the distribution has extended tails indicating the presence of "extreme" radial velocities in both the red and blue parts.

Figure 4 presents the histogram obtained from the investigation of the corrected Hα line widths. A mean dispersion of $\langle \beta_{\rm survey,corr} \rangle = 9.213 \pm 0.002$ km s^{-1} is found, slightly below the sonic regime. This value seems to coincide with an intermediate case scenario between subsonic Hα line widths usually found for Galactic objects and larger, supersonic dispersion values associated with giant extragalactic H II regions (O'Dell & Townsley 1988). The standard deviation of the line-width distribution is found at $\sigma_\beta = 3.889 \pm 0.001$ km s^{-1}. An asymmetry coefficient of 0.66 is obtained, mainly due to a long right tail of dispersion points well above 20 km s^{-1}. However, the left tail stops its progression before reaching 0 count (as would be expected). Actually, about 3% of our Hα spectra (a fraction roughly equivalent to the missing portion of the distribution's left tail) have failed to provide reliable line-width information as the quadratic subtraction method (see Section 3) gave $\beta^2_{i,\rm corr} < 0$ km s^{-1}, which is numerically inadequate. These spectra were rejected from both the Hα line width and LSR radial velocity analysis. The two "fat tails" contribute to a kurtosis excess of 1.23.

In the two following subsections, kinematical evidences for numerous radial velocity and line-width linear gradients will be provided. Each flow is labeled from A to X in Column 2 of Table 4. The range on which each flow remains well defined (i.e., the distance on the plane of the sky over which the slopes of the radial velocity and line-width gradients remain roughly constant) is presented in Column 3. In the text,

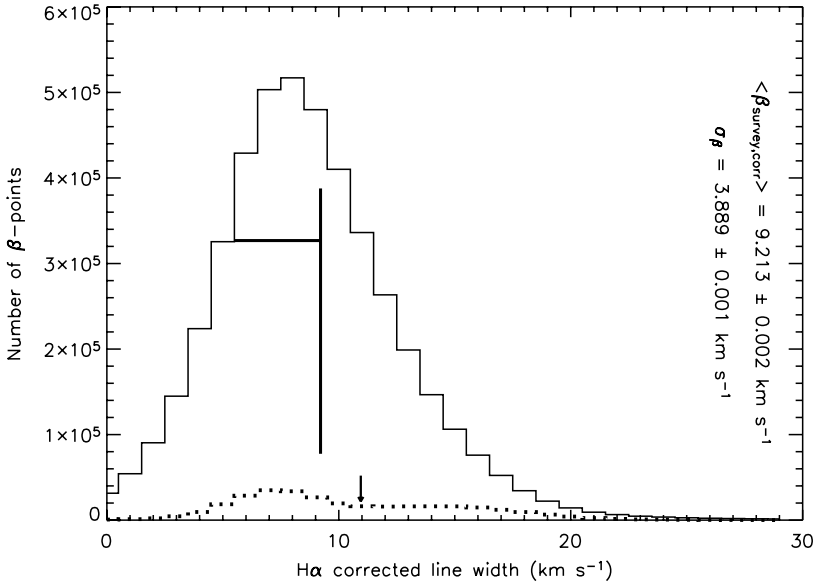

Figure 4. Corrected Hα line-width distribution of W4-south. Both the mean dispersion value and the statistical one standard deviation, found, respectively, at 9.213 ± 0.002 km s^{-1} and 3.889 ± 0.001 km s^{-1}, are schematically represented by the vertical and horizontal thick solid lines. The asymmetry coefficient is estimated at 0.65 and the kurtosis excess is found at 1.23. A normal distribution would give a skewness and a kurtosis excess of 0. The dotted histogram corresponds to the corrected Hα line-width distribution of the interflow medium of W4-south. The mean of the distribution, estimated at 10.95 ± 0.01 km s^{-1}, is indicated by the solid arrow.

Table 4
Kinematical Investigation of Localized Ionized Flows

Field	Flow	Range	LSR Radial Velocities			Hα Line Widths		
		(pc)	∇_v (km s^{-1} pc^{-1})	$v_{k,\mathrm{initial}}$ (km s^{-1})	Correlation	∇_β (km s^{-1} pc^{-1})	$\beta_{k,\mathrm{initial}}$ (km s^{-1})	Correlation
01	A	7.39	−0.31 ± 0.06	−45.13 ± 0.08	−0.92	0.16 ± 0.04	9.30 ± 0.09	0.88
02	B	2.43	−1.43 ± 0.14	−43.98 ± 0.20	−0.81	0.83 ± 0.12	6.79 ± 0.17	0.75
03	C	4.74	−0.58 ± 0.04	−44.06 ± 0.10	−0.90	0.56 ± 0.04	9.21 ± 0.12	0.85
04	D	3.25	1.56 ± 0.19	−44.95 ± 0.49	0.83	2.14 ± 0.05	9.43 ± 0.09	0.93
06	E	3.25	1.29 ± 0.08	−40.54 ± 0.16	0.92	1.21 ± 0.05	8.36 ± 0.10	0.97
06–07	F	4.91	−0.85 ± 0.07	−46.39 ± 0.21	−0.87	−1.69 ± 0.05	15.17 ± 0.16	−0.97
11	G	1.60	1.53 ± 0.27	−43.97 ± 0.25	0.79	−0.87 ± 0.19	8.67 ± 0.18	−0.71
08–09–11	H	1.27	0.76 ± 0.24	−44.45 ± 0.18	0.66	−0.64 ± 0.21	6.52 ± 0.16	−0.57
09–10	I	4.91	0.53 ± 0.03	−49.14 ± 0.09	0.92	−0.07 ± 0.05	8.75 ± 0.13	−0.06
09–10	J	2.43	1.29 ± 0.08	−48.18 ± 0.11	0.95	0.09 ± 0.08	8.03 ± 0.12	0.36
10–14	K	1.60	2.43 ± 0.23	−47.18 ± 0.21	0.93	0.05 ± 0.17	6.73 ± 0.16	0.05
13	L	0.69	−2.60 ± 0.27	−45.43 ± 0.11	−0.96	3.62 ± 0.45	12.28 ± 0.19	0.95
13–14–15	M	1.35	−2.29 ± 0.26	−41.37 ± 0.21	−0.91	1.02 ± 0.06	6.97 ± 0.05	0.97
13	N	0.78	−2.43 ± 0.17	−45.52 ± 0.08	−0.98	3.16 ± 0.28	11.51 ± 0.13	0.98
13–16	O	1.35	−1.33 ± 0.09	−43.95 ± 0.07	−0.97	1.57 ± 0.09	8.96 ± 0.07	0.98
16	P	3.25	−0.09 ± 0.06	−41.96 ± 0.11	−0.30	0.07 ± 0.07	10.20 ± 0.14	0.06
13–14–15	Q	0.94	−0.57 ± 0.10	−41.81 ± 0.06	−0.88	1.97 ± 0.24	7.12 ± 0.14	0.94
13–14–15	R	1.11	−1.88 ± 0.30	−42.21 ± 0.20	−0.87	1.46 ± 0.13	6.74 ± 0.09	0.96
17–18	S	13.01	−0.48 ± 0.04	−39.15 ± 0.30	−0.85	0.11 ± 0.03	5.03 ± 0.24	0.22
17	T	4.91	1.43 ± 0.08	−44.34 ± 0.22	0.94	0.40 ± 0.04	5.00 ± 0.13	0.73
18	U	4.91	1.64 ± 0.04	−47.12 ± 0.12	0.98	0.45 ± 0.08	5.89 ± 0.22	0.66
19	V	2.71	0.12 ± 0.15	−35.52 ± 0.24	0.15	−0.13 ± 0.16	11.74 ± 0.26	−0.15
20	W	4.87	0.13 ± 0.12	−41.15 ± 0.31	0.19	0.22 ± 0.08	11.18 ± 0.22	0.26
20	X	2.54	−1.26 ± 0.47	−33.02 ± 0.72	−0.66	0.59 ± 0.11	9.08 ± 0.36	0.79

end radial velocities and line widths will refer to the radial velocities and line widths observed at the end of these ranges. These values are not presented in Table 4 but can be easily derived from the information provided. The radial velocity and line-width behaviors are, respectively, given in Columns 4–6 and Columns 7–9. Table 4 provides the steepness of each linear gradient (∇_v and ∇_β), the Y-intercept value for each relation ($v_{k,\mathrm{initial}}$ and $\beta_{k,\mathrm{initial}}$ with k being labeled between A and X in the text), and the Pearson correlation coefficients (Bevington 1969, Chapter 4) derived from least-squares fits applied to the straight lines. For the radial velocity investigation, a radial velocity gradient characterized by a positive (negative) slope will be referred to as a redshifted (blueshifted) tendency with respect to its Y-intercept value, $v_{k,\mathrm{initial}}$, the LSR radial velocity of the ionized gas in contact with the neutral material. Similarly, a positive (negative) slope related to a particular line-width gradient will be associated with a tendency toward line broadening (narrowing) compared to its Y-intercept, $\beta_{k,\mathrm{initial}}$.

Table 5
Kinematical Comparison Between the Spatially Coinciding Neutral and Ionized Material

Flow	Nature	$v_{k,\mathrm{neutral}}$ (km s^{-1})	$v_{k,\mathrm{initial}}$ (km s^{-1})	$\beta_{k,\mathrm{initial}}$ (km s^{-1})	Extrapolation (pc)	Source
A	Molecular	−44.0	−45.13 ± 0.08	9.30 ± 0.09	...	1
B	Molecular	−45.0	−43.98 ± 0.20	6.79 ± 0.17	...	1
C	Molecular	−46.0	−44.06 ± 0.10	9.21 ± 0.12	...	1
D	Atomic	[−42.0, −46.0]	−44.95 ± 0.49	9.43 ± 0.09	...	2
E	Molecular	−40.0	−40.54 ± 0.16	8.36 ± 0.10	...	1
F[a]	Molecular	−43.0	−44.5	19.0	2.25	1
G	Molecular	−43.5	−43.97 ± 0.25	8.67 ± 0.18	...	1
H	Molecular	−51.0	−44.45 ± 0.18	6.52 ± 0.16	...	1
I[a]	Molecular	[−45.0, −49.0]	−49.8	8.8	1.24	1
J[a]	Molecular	[−45.0, −49.0]	−50.8	7.8	2.06	1
K[a]	Molecular	[−45.0, −49.0]	−50.4	6.7	1.33	1
L	Molecular	[−38.0, −43.0]	−45.43 ± 0.11	12.28 ± 0.19	...	1, 3
M	Molecular	−42.0	−41.37 ± 0.21	6.97 ± 0.05	...	1, 3
N	Molecular	[−38.0, −43.0]	−45.52 ± 0.08	11.51 ± 0.13	...	1, 3
O	Molecular	−42.5	−43.95 ± 0.07	8.96 ± 0.07	...	1, 3
P	Molecular	−41.0	−41.96 ± 0.11	10.20 ± 0.14	...	1
Q	Molecular	−42.5	−41.81 ± 0.06	7.12 ± 0.14	...	1, 3
R	Molecular	−42.0	−42.21 ± 0.20	6.74 ± 0.09	...	1, 3
T	Atomic	[−43.0, −47.0]	−44.34 ± 0.22	5.00 ± 0.13	...	2
U	Atomic	[−43.0, −47.0]	−47.12 ± 0.12	5.89 ± 0.22	...	2
V	Molecular	−37.0	−35.52 ± 0.24	11.74 ± 0.26	...	1, 3
W	Molecular	[−28.0, −32.0]	−41.15 ± 0.31	11.18 ± 0.22	...	1
X[a]	Molecular	[−28.0, −32.0]	−31.0	8.2	1.50	1

Note. [a] Flows F, I, J, K, and X required an extrapolation of their origin on a certain range to their associated molecular cloud fragment. Source 1: FCRAO CO (1–0) observations (Heyer et al. 1998). Source 2: CGPS H I observations. (Normandeau et al. 1997) Source 3: JCMT CO (2–1) observations (Taylor et al. 1999)

Except for Flow S, each flow in Table 4 is chosen supposing a probable Champagne flow and is therefore traced out, as far as possible, such that its origin coincides with ionized material in contact with the eroded neutral feature. Table 5 presents a comparison in radial velocities between the neutral material (its nature, atomic or molecular, being given in Column 2) and this ionized component, respectively, in Columns 3 and 4. Column 4 corresponds to Column 5 of Table 4 except for Flows F, I, J, K, and X where an extrapolation from the origin of each flow to their associated molecular fragment was necessary (see Section 4.2). For these flows, the line-width gradient was also extrapolated, giving the new $\beta_{k,\mathrm{initial}}$ values in Column 5. The $\beta_{k,\mathrm{initial}}$ values remain unchanged with respect to Table 4 if no extrapolation is necessary. The range on the plane of the sky corresponding to the extrapolation is estimated in Column 6. The source of the radial velocities presented in Column 3 is given in Column 7. All radial velocities in Table 5 are measured with respect to the LSR.

4.2. Ionized Gas's Kinematics in the Vicinity of Molecular Material

In order for the reader to identify (spatially) each flow in the context of W4-south, Hα peak intensity maps (i.e., for each pixel, the maximum photon counts obtained from the Gaussian fit procedure once the continuum properly subtracted) have been obtained for each field. Fields enclosing ionized gas flows likely related to the photoerosion of nearby molecular clumps are presented in Figures 5(a)–(c), 6, and 8, whereas Figures 5(d) and 7, related to the photoerosion of H I material, will be discussed in Sections 4.3 and 5.3. The disposition of Fields 06–16, 19, and 20 allows us to obtain mosaicked images for Figures 6 and 8. Obvious lines of demarcation can be seen separating each field. This is mainly due to differences in exposure times and sky transparency. To avoid confusion, numbers used for field identification were voluntarily omitted in Figure 6. The reader can refer to Figures 1 and 2 to deduce the location of each field in the mosaicked image.

Each flow is properly identified by its appropriate letter (see Tables 4 and 5). The "slice-of-a-pie" regions enclose the pixels used in the investigation of each flow. Radial velocity and line-width gradients are always measured from "the center" to "the crust". In Figure 5, dotted lines indicate the orientation of the ionized shell. The bottom-right corner of Figure 6 coincides approximately with the star cluster IC 1805. Thirteen OB stars are drawn from the positions indicated by Massey et al. (1995). In many cases, the presence of molecular material (see Figure 2) at the origin of particular flows is clearly unmistakable from bright Hα rims pinpointing ionization fronts. Figure 9 is added to this work in order to visualize the presence or not of molecular material in the vicinity of Fields 17–19 (all located above the northern latitude of Figure 2). Even though Figure 2 clearly indicates the presence of molecular clumps, some sections of our FPI observations do not, a priori, show the same characteristic in Hα; the absence of bright rims was mitigated by adding black squares in Figures 5(a) and 8 at the position of molecular material (estimated from the FCRAO CO (1–0) observations).

The following results exclusively apply to ionized flows presenting a molecular nature in Column 2 of Table 5. The behavior in radial velocities has shown well-defined linear gradients pointing away from the individual cloud fragments (see Table 4). The kinematical tendency alternates between blueshifted and redshifted. In absolute value, the radial velocity slopes are found between 0.31 and 2.60 km s^{-1} pc^{-1}, all below the maximal Champagne gradient predicted (see Section 1). The most common trend is toward line broadening

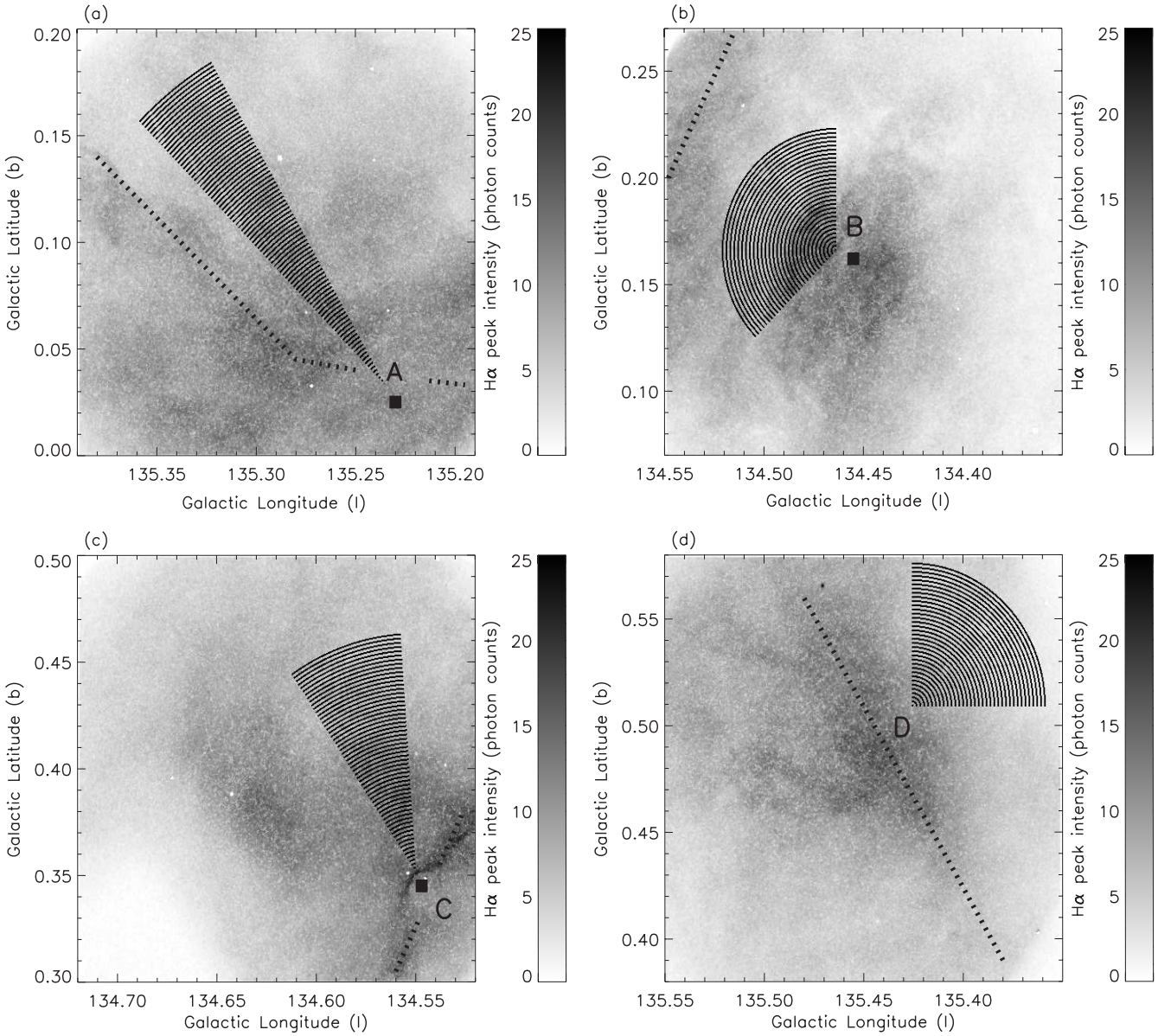

Figure 5. Hα peak intensity maps for (*a*) Field 01, (*b*) Field 02, (*c*) Field 03, and (*d*) Field 04. Areas investigated for Flows A to D are represented by the "slice-of-a-pie" regions. Black filled squares coincide with the location of molecular material according to the FCRAO CO (1–0) observations. The dotted lines indicate the orientation of the ionized shell.

even though Flows F, G, and H, near the star cluster, show a line narrowing behavior (see Table 4). The line-width slopes are usually below 2 km s^{-1} pc^{-1} with peak values slightly above 3 km s^{-1} pc^{-1} for Flows L and N in the vicinity of the molecular fragment G134.9+1.4. The $\beta_{k,\mathrm{initial}}$ values, in contact with the molecular material, usually indicate a subsonic regime. However, supersonic values above 10 km s^{-1} are found for Flows L, N, and P, also associated with G134.9+1.4. A similar regime for Flows V and W is also observed near G134.6+1.9.

Unfortunately, it was not possible to extract precise kinematical information at the intersection of Fields 06 and 07 due to instrumental vignetting. Therefore, Flow F was investigated from an origin located slightly beyond the south-east boundary of Field 06 (see Figure 6). Extrapolation of the radial velocity gradient on the missing range to the extremely emissive Hα feature in Field 06 (estimated at 2.25 pc) leads, for the extended Flow F, to a new value for $v_{F,\mathrm{initial}}$ near −44.5 km s^{-1} (see Table 5). This feature is particularly interesting as no molecular counterpart can be seen in Figure 2 (if not for really faint emission below 5 K km s^{-1} barely deduced from the FCRAO CO (1–0) observations). We, therefore, interpret the emissive structure as an old molecular fragment that has undergone almost full erosion. An extrapolation of Flows I, J, K, and X was also necessary since the associated molecular fragments are, respectively, located beyond the eastern and western boundaries of Fields 08–10 and 20 (see Figure 2). New extrapolated *Y*-intercept values (in radial velocities and line widths) are also presented in Table 5.

4.3. Ionized Gas's Kinematics in the Vicinity of Atomic Material

Along the eastern wall of W4-south, Fields 04, 17, and 18 investigate at eroded shell segments likely formed of compressed atomic material. A faint molecular fragment seems to be detected slightly south of Field 18 in Figure 9 but has been ruled out since its radial velocity, near −60 km s^{-1}, does not match the kinematics of Flow S in Table 4. The small CO clump is, therefore, likely located well in front or behind W4-south.

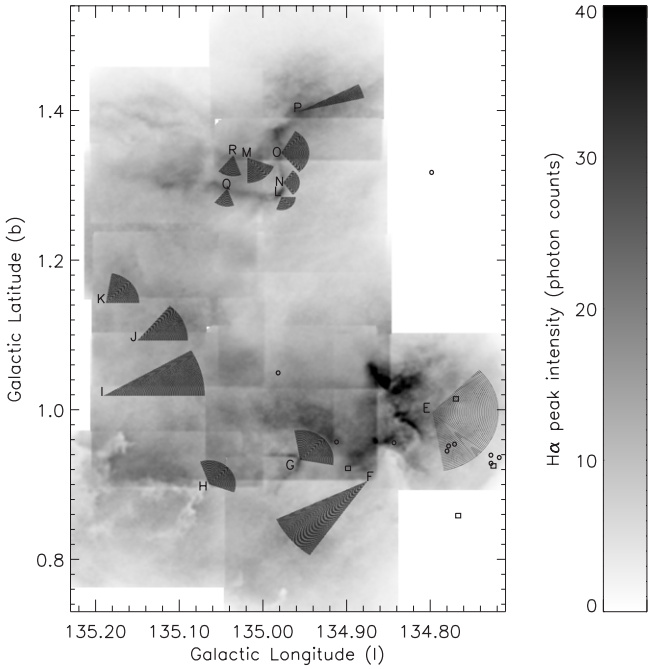

Figure 6. Mosaicked Hα peak intensity map for Fields 06–16. Open squares (circles) coincide with massive O stars (B stars) associated with the star cluster IC 1805. B stars were considered only for spectral types B0 and B1. At least, eight other massive stars, with spectral types ranging between O7 and B1, are not shown in the mosaicked image ($l < 134.^{\circ}71$). The reader is referred to Figures 1 and 2 in order to identify the location of the 10 fields. Areas investigated for Flows E to R are represented by the "slice-of-a-pie" regions.

Figures 5(d) and 7 present the Hα peak intensity maps for the three fields. Dotted lines again indicate the orientation of the ionized shell.

Flows D (Field 04), T (Field 17), and U (Field 18) all present a roughly identical behavior in radial velocities. The gradients are estimated at roughly 1.5 km s^{-1} pc^{-1} along redshifted tendencies directed from the shell toward the center of the expanding bubble (see Table 4). For all three flows, the end radial velocities are found slightly above −40 km s^{-1}. Correlated to the radial velocity gradients, line broadening is observed similar to the majority of the flows presented in Section 4.2. The line-width slope is, however, much steeper in Flow D when compared to Flows T and U. In every case, the $\beta_{k,\mathrm{initial}}$ values remain in the subsonic regime. A behavior similar to Flows, D, T, and U can be observed in the southern portion of Field 03 (below Flow C in Figure 5(c)), but was not retained for Tables 4 and 5.

The mosaicked image of Figure 7 allows us to investigate the kinematical behavior of the eroded shell on a 13 pc range along the eastern wall of W4-south. Flow S shows a relatively flat but well-defined radial velocity gradient. The tendency is blueshifted along a "south-to-north" axis with radial velocities ranging from roughly −39 to −46 km s^{-1} near the origin of Flow U. The line-width behavior shows the ionized material (in contact with the expanding shell) with dispersion values roughly constant between 5 and 6 km s^{-1}.

Even though the ionized shell dominates the emission in both Fields 17 and 18, weaker filamentary structures can be seen near the southern portion of Figure 7 ($135.^{\circ}5 \leqslant l \leqslant 135.^{\circ}6$, $b \leqslant 1.^{\circ}75$). Relatively parallel to each other, the filaments are kinematically linked to the inner and brighter ionized shell with roughly identical radial velocities, approaching −40 km s^{-1}, centered on $b = 1.^{\circ}73$.

4.4. Interflow Medium

Many areas of our Hα survey of W4-south have shown no indication of well-defined radial velocity and line-width gradients. These areas are referred to as the interflow medium in a sense that the ionized material is not specifically related to the photoerosion of a particular neutral feature, atomic or molecular. We identify these zones as the western portion of Field 05, Field 12, the southern portion of Fields 13 and 14, the eastern portion of Field 15, the northern portion of Field 16, and the eastern portion of Field 20. The eastern portion of Field 05 was not considered since the northern tip of a well-defined vertical filament of ionized material is detected (see Figure 2). The horseshoe-shaped structure undoubtedly points toward the star cluster. The filament's origin, roughly 15 pc below Field 05, is located slightly beyond the western boundary of Field 01 near the southern polar cap of W4. The enhanced Hα emission presents roughly constant radial velocities between −37 and −40 km s^{-1} and particularly low line widths slightly below 5 km s^{-1}.

The LSR radial velocity and corrected line-width distributions of the interflow medium are, respectively, shown in Figures 3 and 4 as the dotted histograms. In both figures, the black arrow indicates the position of the mean value of the distribution: $\langle v_{\mathrm{interflow,LSR}} \rangle$ and $\langle \beta_{\mathrm{interflow,corr}} \rangle$ are, respectively, estimated at -38.04 ± 0.01 km s^{-1} and 10.95 ± 0.01 km s^{-1}. The interflow medium, with a mean S/N of 35, is slightly more tenuous than the remaining of the ionized material investigated in our Hα survey of W4-south (which presents a mean S/N of 44). Both the radial velocity and line-width distributions present particularly large asymmetry coefficients estimated, respectively, at 0.47 (toward the red tail of radial velocities) and 0.56 (toward the right tail of supersonic line widths). The zones used in our definition of the interflow medium correspond to roughly 12% of the total area covered by Fields 01–20.

5. DISCUSSION

5.1. General Overview

Investigation of the FCRAO CO (1–0) survey has revealed a mean LSR radial velocity of -47.2 ± 3.5 km s^{-1} for the molecular material observed in the vicinity of the W4 superbubble ($\langle v_{\mathrm{FCRAO,CO}} \rangle$). Our value for $\langle v_{\mathrm{survey,LSR}} \rangle$ is, therefore, redshifted by nearly 5 km s^{-1} (see Section 5.4) compared to the last fragments of the giant molecular cloud that likely gave birth to W4. The standard deviation of the radial velocity distribution in Figure 3 presents a particularly small value considering the imposing dimensions of the superbubble. More important spreadings in radial velocities have been obtained from the Hα investigation of much smaller Galactic H II regions. The comparison is, however, debatable since the geometry of a given object will largely influence the kinematical disorder observed on the plane of the sky. For example, the Sh 2-158 H II region presents an Hα emissive component over a small area of 30 pc^2 and a 1σ deviation of its LSR radial velocity distribution estimated at 7.80 ± 0.02 km s^{-1} (Barriault & Joncas 2007). Since Sh 2-158 has an inclination of 60° with respect to the LOS, accelerated flows, therefore, present noticeable variations in radial velocities on surprisingly small distances. A similar argument can be used for the Sh 142 H II region (Joncas & Roy 1984) and the M17 nebula (Joncas & Roy 1986) presenting inclinations with respect to the LOS, respectively, estimated at 45° and 0° and radial velocity distributions characterized by standard deviations of 12.5 and 10.1 km s^{-1}. However, the Sh 269 H II region

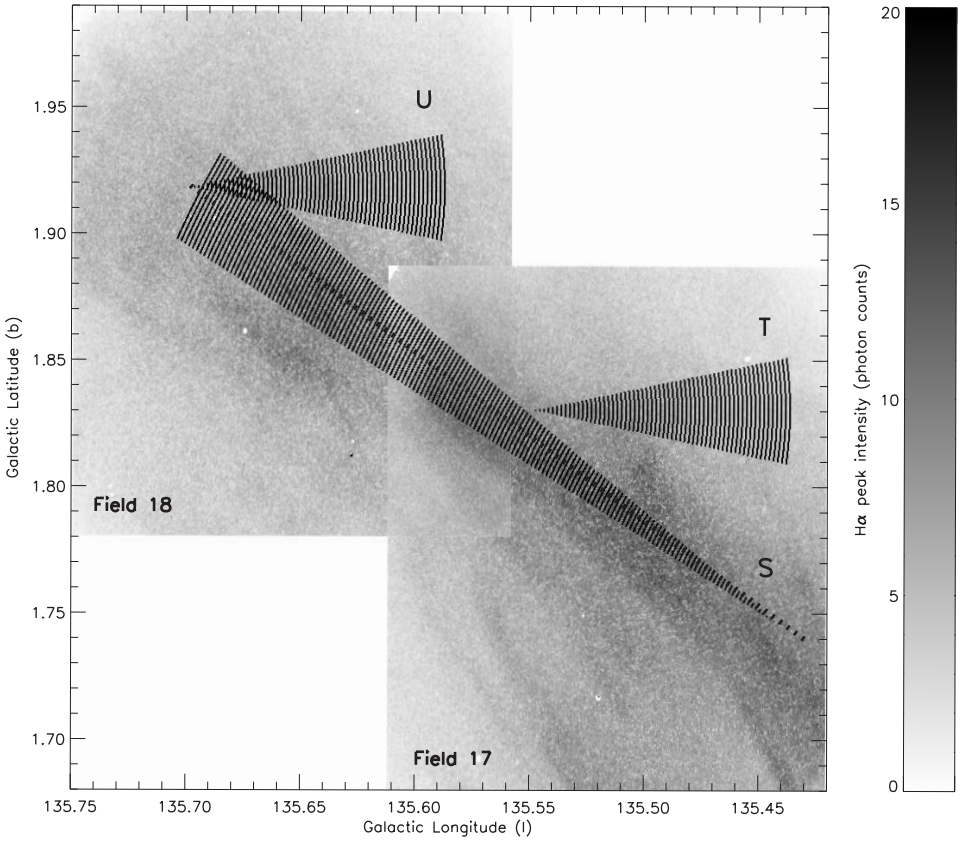

Figure 7. Mosaicked Hα peak intensity map for Fields 17 and 18. Areas investigated for Flows S to U are represented by the "slice-of-a-pie" regions. The dotted line indicates the orientation of the ionized shell.

(Godbout et al. 1997), characterized by a face-on view, presents an inclination of roughly 90°, almost perfectly perpendicular to the LOS, and an extremely narrow distribution with a 1σ deviation estimated at 2.77 km s^{-1}. The relatively narrow radial velocity distribution of W4 might, therefore, be attributed to gas flows found mostly parallel to the plane of the sky, artificially attenuating the steepness of small-scale radial velocity gradients. This is likely related to a small angle of inclination (of the W4 superbubble) with respect to the plane of the sky (see Paper II).

The mean line width, slightly below 10 km s^{-1}, of our Hα survey suggests a rather complex kinematical behavior, along the LOS, of the ionized material embedded in W4-south. The fact that $\langle \beta_{\rm survey,corr} \rangle$ lies between subsonic and supersonic regimes is of great interest. Considering dimensions of the kiloparsec order for extragalactic H II regions, supersonic line widths could easily be explained through very complicated velocity systems (O'Dell & Townsley 1988). Embedded OB associations, being found dispersed in a single object, could lead to the mixing of numerous ionized flows provoked by the hydrodynamical interaction of stellar winds and the photoerosion of numerous molecular clouds. For giant H II regions encompassing a large amount of ionized material, this would likely result in a turbulent hot interior with an important overlap of strong radial velocity gradients along the LOS (Rosa & Solf 1984; Hippelein & Fried 1984). The link between small-size (< 30 pc) Galactic and giant (> 500 pc) extragalactic H II regions could, therefore, be provided by W4-type superbubbles.

Table 1 shows no indication for a large-scale radial velocity gradient pointing toward the Galactic corona, a kinematical behavior expected from the chimney model (Section 1). The $\langle v_{i,\rm LSR} \rangle$ values are all, except for Field 19, within 1σ ($\pm$ 5.204 km s^{-1}) of $\langle v_{\rm survey,LSR} \rangle$ (see Figure 3). The variations in radial velocities are, therefore, negligible to conclude for a large-scale trend. Either the chimney model does not allow us to properly interpret the kinematics of the ionized material enclosed in W4-south or a large-scale flow could be present but undetectable, perfectly parallel to the plane of the sky. This demands the W4 superbubble to be seen face-on with a 90° inclination. In Section 5.2, we confirm W4 as being slightly tilted toward the observer and, therefore, reject the latter assumption.

5.2. Ionized Gas's Kinematics in the Vicinity of Molecular Material

Using the values and signs of the different radial velocity slopes presented in Column 4 of Table 4, a spatial scenario presenting the distribution of the molecular material along the LOS of W4-south has been obtained. The details, and particularly how ∇_v values in Table 4 provide an estimate of the angle of each flow with respect to the LOS, will be presented in Section 6. However, the reader can already refer to Figure 11 in order to have in mind a large-scale view of the CO distribution for the discussion to follow.

From Table 5, flows presenting a molecular nature in Column 2 have shown (in most cases) striking similitudes between $v_{k,\rm neutral}$ and $v_{k,\rm initial}$. This is in agreement with the Champagne model in which freshly ionized material initially retains the kinematics of the eroded material before being accelerated due to the pressure discontinuity (see Section 1). This argument confirms the observed kinematics as being roughly explained by a series of small-scale Champagne flows crisscrossing the nebula. Moreover, a possible contribution attributed to stellar winds

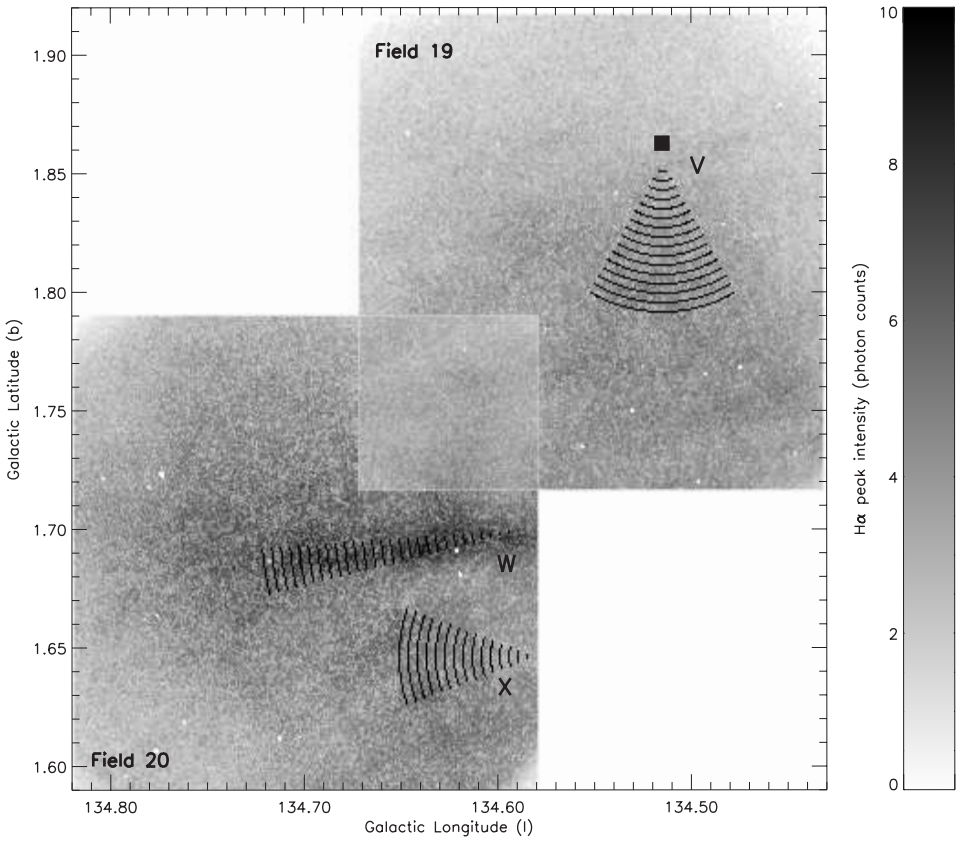

Figure 8. Mosaicked Hα peak intensity map for Fields 19 and 20. Areas investigated for Flows V to X are represented by the "slice-of-a-pie" regions. The black filled square coincides with the location of molecular material according to the JCMT CO (2–1) observations.

cannot be properly identified from the low ∇_v values in Table 4. Comerón (1997) has shown Champagne flows, boosted by the addition of stellar winds, to present radial velocity gradients slightly steeper than the maximal gradient originally predicted by Bodenheimer et al. (1979). Therefore, two possibilities arise: (1) the stellar winds have only a negligible contribution on the kinematics of the ionized material or (2) supposing stellar winds to have a sizeable impact on the different flows, the particular geometry of W4-south does not allow us to observe important variations in radial velocities on the plane of the sky and, therefore, steeper gradients (see Section 5.1).

Intuitively, we would expect the ionized material in contact with the individual cloud fragments to present initial line widths in a subsonic regime, an assumption motivated by extremely narrow line widths usually obtained from the CO observations (Blitz et al. 1982; Digel et al. 1996; Lee et al. 1999). Flows L and N associated with the cloud fragment G134.9+1.4 present an interesting case in which supersonic values for $\beta_{k,\mathrm{initial}}$ are obtained (addressed below). From Table 4, the line broadening behavior ($\nabla_\beta > 0$) is also in agreement with the Champagne model (see Section 1). Many explanations are proposed for larger line widths down the Champagne flows. In particular, a sizeable source of broadening can be attributed to the growing depth of the W4 superbubble as the progression is made away from the small clump toward the star cluster; the constant increase of the investigated volume of embedded ionized material accentuates the probability of finding numerous ionized flows along the LOS, a kinematical contribution to line broadening. In particular for Flow C (see Figure 5(c)), the investigated depth across the W4 superbubble is estimated to vary from roughly 0 (near the shell) to 28 pc at a distance of 4.74 pc from the shell (assuming a radius of 24 pc between the molecular fragment and the star cluster). This diversity of flow may well be exacerbated by the ruggedness of the neutral fragment's surface. A molecular clump showing irregular, ragged edges could lead to a series of individual Champagne flows presenting slight differences in inclination with respect to the LOS. Roughly indistinguishable at the pressure discontinuity, this could possibly lead to an important broadening on a range of a few parsecs. This argument is expected for Flow B since the enhanced Hα emission in Figure 5(b) shows evidences of bumps and holes at the periphery of the molecular fragment (Felli et al. 1977). The porosity of the eroded material could additionally amplify the line splitting predicted in the modelization of Champagne flows (see Section 1). The spectral resolution of the FaNTOmM device system does not, however, allow us to detect evidences of line splitting. Finally, for molecular fragments in the immediate vicinity of the star cluster, line broadening can be due to numerous nearby sources of ionization. The approximation of an ionizing point source does not hold for Flow E where each star will likely initiate its own Champagne flow characterized by its own radial velocity gradient. In fact, this argument also applies to the radial velocity gradient where a mean value is determined.

Immediately, conclusive results can be deduced from Table 4. If we limit ourselves to the investigation of molecular clumps found exclusively at the boundaries of the H II region, a change of sign in the radial velocity gradients is observed from Flows A, B, and C to Flows I, J, and K. Normandeau et al. (1996) introduced the W4 H I supershell as being slightly tilted toward the observer (see Section 1). Assuming the center of rotation to coincide with the vicinity of star cluster IC 1805,

a large fraction (> 50%) of the superbubble's volume above (below) $b = 0.^{\circ}9$ should be located in front of (behind) the ionizing sources. This said, the majority of the cloud fragments found compressed on the outer shell should also be located in front or behind the star cluster depending on their latitude, above or below $b = 0.^{\circ}9$. Table 4 clearly confirms this behavior as Flows A, B, and C all indicate blueshifted tendencies related to forward accelerated flows and, therefore, molecular clumps found near the rear wall of W4-south (see Figure 11). Above the $b = 0.^{\circ}9$ threshold, Flows I, J, and K are associated with a large cloud fragment likely located in front of the ionizing sources as seen from the positive ∇_v values. This tends to confirm the W4 superbubble as being clearly tilted toward the observer. Moreover, supposing the cloud fragment associated with Flows I, J, and K as being also tilted toward the observer, a change in the angle of each flow with respect to the LOS is expected as one moves from $b = 1.^{\circ}0$ to $b = 1.^{\circ}2$ (see Figure 11). This is assumed supposing each flow to be roughly oriented toward the star cluster. Kinematically, this results in radial velocity gradients more and more steeper from Flows I to J and from Flows J to K (see Table 4).

The behavior in radial velocities for Flows F and G is perfectly in agreement with the expectations of the Champagne model. The discrepancy $v_{H,\mathrm{neutral}}$ versus $v_{H,\mathrm{initial}}$ for Flow H (see Table 5) can be easily explained from the *V*-shaped absorption band at the location of the molecular fragment (see Figure 6). The latter is thus at a relatively large distance in front of the ionizing sources (probably beyond the boundaries of the H II region) since it blocks the W4-south Hα emission. The measurement of Flow H starts when it is already far from the neutral fragment. Extrapolating the gradient in order to obtain an initial radial velocity of -51 km s^{-1} (to coincide with the molecular material) demands the flow to have traveled roughly 9 pc before it "appears" near the western boundary of the molecular cloud. However, the three flows (F, G, and H) are all characterized by line narrowing gradients (see Table 4). Flow collimation is certainly not expected from the Champagne model (see Section 1). Even though the discrepancy seems to diminish in Flows I to K, negative ∇_β values are quite surprising. The simplest explanation for such collimation might reside in an important loss of kinematical information along the LOS due to absorption (induced by interstellar dust). From Figures 3–16 of West (2003), the 60 μm *Infrared Astronomical Satellite* (*IRAS*) image of the W3/W4/W5 complex shows particularly bright emission in the vicinity of the star cluster IC 1805.

The molecular fragment G134.9+1.4 represents a particularly complicated case. As predicted by Taylor et al. (1999), the sign of the radial velocity slopes for Flows L to R in Table 4 confirms the cloud as being located behind the star cluster. Combined to supersonic values obtained for $\beta_{L,\mathrm{initial}}$ and $\beta_{N,\mathrm{initial}}$, the slight discrepancies in radial velocities $v_{L,\mathrm{initial}}$ versus $v_{L,\mathrm{neutral}}$ and $v_{N,\mathrm{initial}}$ versus $v_{N,\mathrm{neutral}}$ are best explained by numerous ionized flows along the LOS of the fragment's southern tip. Above the bright ionization front seen in the northern portion of Figure 6, a secondary Hα rim is observed at the junction of Fields 13, 15, and 16, evidence of a molecular fragment not entirely smoothed out by tangential ionizing photons. Eroded material is, therefore, expected to flow from this secondary rim toward the southern tip of the cloud fragment. The value measured for $v_{M,\mathrm{initial}}$, this time, coincides with the radial velocities of the molecular material (see Table 5). A similar conclusion is reached for $\beta_{M,\mathrm{initial}}$, as expected, in the subsonic regime (see Table 5). Extrapolating the line broadening gradient to the origin of Flow L (i.e., to extend the range of Flow M in Table 4 from 1.35 to 2.72 pc) leads to end line widths of 9.8 km s^{-1}, roughly 2.5 km s^{-1} narrower than the value predicted by $\beta_{L,\mathrm{initial}}$. The difference mainly results from the erosion of the fragment's southern tip and its associated ionized flow that "adds up" to the accelerated material observed in Flow M, a model that contributes for a sudden broadening excess. A direct comparison between $v_{L,\mathrm{initial}}$ and the radial velocities of the (spatially) corresponding molecular material in Table 5 is, therefore, inappropriate since the *Y*-intercept value is clearly contaminated by northern flowing material. The end radial velocities of the extended Flow M are -47.6 km s^{-1} at the origin of Flow L, blueshifted by more than 2 km s^{-1} from $v_{L,\mathrm{initial}}$. If we assume Flow L to result from the merging of Flow M and the accelerated ionized flow (now referred as Flow L*) anticipated from the photoionization of the fragment's southern tip, we propose $v_{L,\mathrm{initial}}$ to roughly equal $0.5\times (v_{M,\mathrm{end}} + v_{L^*,\mathrm{initial}})$. This gives $v_{L^*,\mathrm{initial}} = -43.3$ km s^{-1}, in agreement with $v_{L,\mathrm{neutral}}$ in Table 5. This simple model would explain why $v_{L,\mathrm{initial}}$ is blueshifted with respect to the molecular material. Moreover, since ∇_v for Flow L can be interpreted as a mean between the radial velocity gradients of Flows L* and M, we propose the former to be characterized by a steep gradient near -2.90 km s^{-1} pc^{-1} (in order to compensate for the "slowdown" brought by the latter). This value is almost in agreement with the maximal Champagne gradient theoretically predicted (see Section 1). Similar "back-to-the-envelope" calculations connecting Flows M and N give $v_{N^*,\mathrm{initial}} = -43.6$ km s^{-1} and a radial velocity gradient of -2.57 km s^{-1} pc^{-1}. Finally, from $v_{O,\mathrm{initial}}$ ($\sim v_{L^*,\mathrm{initial}}$, $\sim v_{N^*,\mathrm{initial}}$) and $\beta_{O,\mathrm{initial}}$ (< 10 km s^{-1}) in Table 4, we assume Flow O to remain uncontaminated by Flow M. A clear change in the angle of view along the western edge of G134.9+1.4 is, however, deduced from more and more flatter radial velocity slopes from Flows L* to N* and from N* to O. A similar argument also applies to the eastern edge of the cloud fragment along which Flow Q remains apparently unaffected by Flow R. As for Flow O, the two flows present initial line widths well in the subsonic regime and initial radial velocities in agreement with the FCRAO CO (1–0) and JCMT CO (2–1) observations (see Table 5).

The northernmost neutral feature associated with W4-south coincides with the molecular fragment G134.6 + 1.9. In their investigation of the CO (2–1) transition, Taylor et al. (1999) particularly noticed the apparent lack of continuum emission in its vicinity and the absence of ionization fronts at its periphery. This, obviously, is in agreement with the detection of particularly weak Hα lines throughout Fields 19 and 20. Combined effects of geometrical dilution of the UV flux and the photoabsorption of energetic photons at lower latitudes are proposed as an explanation. Assuming a weak photoionization to take place behind the cloud fragment, this could explain the absence of bright Hα rims in Field 19. The origin of Flow V (see Figure 8) roughly coincides with the southern tip of G134.6+1.9's Feature II according to the notation used by Taylor et al. (1999) (see the authors' Fig. 2(b)). Table 5 gives $v_{V,\mathrm{initial}}$ roughly in agreement with $v_{V,\mathrm{neutral}}$. However, Table 4 provides no indication for accelerated ionized material in Flow V. A Champagne flow observed roughly parallel to the plane of the sky is ruled out since it would likely induce a well-defined line broadening gradient. Instead, the line-width behavior shows a relatively constant and supersonic regime from the optical center of Field 19 to its southern boundary, mostly in agreement with the interflow medium (see Section 5.4).

Therefore, the kinematics of Field 19 does not reveal any sign for the photoerosion of the molecular fragment G134.6+1.9.

According to the FCRAO CO (1–0) observations, a southern extension of the roughly circular Feature I of Taylor et al. (1999) (see the authors' Fig. 2(b)) is detected beyond the western boundary of Field 20 (see Figure 2). Flow X investigates the erosion of the cloud's eastern edge and reveals a kinematics very similar to Flow O (see above). The sign of the radial velocity slope (see Table 4) indicates a molecular fragment likely located behind the ionizing sources as opposed to the spatial scenario initially proposed by the JCMT CO (2–1) observations (see Section 2). Similar to Flow H, Flow W presents an important discrepancy (~ 10 km s^{-1}) in radial velocities between $v_{W,\mathrm{initial}}$ and $v_{W,\mathrm{neutral}}$ (see Table 5). This can be explained if the photoerosion of the horizontal molecular filament (see Figures 2 and 8) induces a forward ionized flow roughly parallel to the LOS. This scenario is also in agreement with Hα line widths slightly greater than expected along the filament (see Table 4). A similar explanation is also proposed for Flow P (see Figure 6) even though the discrepancy in radial velocities between $v_{P,\mathrm{initial}}$ and $v_{P,\mathrm{neutral}}$ is less obvious (see Table 5).

5.3. Ionized Gas's Kinematics in the Vicinity of Atomic Material

In Section 4.3, kinematical results for Fields 04, 17, and 18 were presented as being roughly similar, all three fields being characterized by an emissive Hα shell likely formed of eroded atomic material. As for the majority of Champagne flows (see Section 5.2), Table 5 presents $v_{D,\mathrm{initial}}$, $v_{T,\mathrm{initial}}$, and $v_{U,\mathrm{initial}}$ roughly in agreement with the radial velocities of the atomic counterpart. In each case, the eroded material, extracted from the compressed shell, flows toward the center of the expanding bubble along redshifted radial velocity gradients with respect to the outer H I component (see Table 4). In every case, tendencies toward line broadening are also observed (see Table 4). Rather than being interpreted as (roughly) identical Champagne flows, such similarities between Flows D, T, and U could be explained if each field (04, 17, and 18) is dominated by a process generalized to the whole H I supershell. The column densities of the atomic shell segments observed in all three fields are roughly equivalent ($\sim 9 \times 10^{20}$ cm^{-2} (K km s^{-1})$^{-1}$) leading, for a shell thickness between 10 and 20 pc (West 2003), to particle densities between n(H I) = 15 cm^{-3} and 30 cm^{-3}. These particle densities remain well below the expected densities (> 100 cm^{-3}) found on the outer envelope of typical molecular clouds (Kutner 1984). We, therefore, assume the pressure difference between the photoionized atomic shell and the embedded ISM to be insufficient in order to carry the eroded material along well-defined Champagne flows. However, the kinematics of Flows D, T, and U could be explained by lagging material, once extracted from the neutral shell, left behind the advancing (toward the observer) supershell. This assumption is best explained with the analogy of a solid body moving in a viscous fluid and the expected dynamics found in its wake (Landau & Lifshitz 1987, Chapter 2). The velocity of the fluid particles in the wake decreases with increasing distance to the solid body (here, the neutral shell). This is related to the monotonic dissipation of the kinetic energy due to viscosity. This model is in agreement with the "shell-to-interior" redshifted radial velocity gradients of Flows D, T, and U, which should, therefore, be interpreted as decelerated flows rather than accelerated flows directed toward the rear wall of W4. This decelerating material, therefore, has a sizeable contribution to the asymmetry coefficient found in the radial velocity distribution of Figure 3 (see Section 4.1) and will be referred to as a sizeable source for the interflow medium (see Section 5.4). A similar interpretation of lagging material, associated with the molecular fragment G134.9+1.4, was proposed by Taylor et al. (1999) in order to explain radial velocity gradients obtained from the JCMT CO (2–1) observations.

Another argument in favor of a generalized tendency associated with the erosion of the H I supershell comes from the apparent tilt of the W4 superbubble. In Section 5.2, we obtained evidences for W4 being slightly tilted toward the observer with the star cluster IC 1805 probably acting as the center of rotation. This was deduced from Champagne flows, initiated at the periphery of the expanding H II region and located above (below) the star cluster, being accelerated away from (toward) the observer. It could, therefore, be assumed that a similar pattern (a change of sign in the radial velocity gradients above and below $b = 0.^\circ9$) should be observed between Flow D and Flows T and U if we choose to categorize them as Champagne flows. Obviously, this is not the case here.

The line broadening gradients observed along the three flows could be partially explained by the "shell-to-interior" geometrical effect related to the constant increase of the investigated volume of ionized material along the LOS (an argument also mentioned in Section 5.2). Flow instabilities can also form, intuitively related to line broadening. In particular, turbulence driven by Kelvin–Helmholtz instabilities is likely to develop in ionized flows assuming a plasma's magnetic field roughly below 10 μG (Watson et al. 2004). From depolarization observations, West et al. (2007) presented estimates between 4 and 7 μG for the magnetic field inside the W4 supershell. Finally, vortex shedding is said to develop with time in uniformly decelerated flows (Wang & Dalton 1991).

In Table 4, the important discrepancy between the line-width slopes of Flow D and Flows T and U could be related to the particle density of the eroded shell. In fact, the particle density of the atomic shell in Fields 17 and 18 is likely below 15 cm^{-3} since the curvature of the shell is probably much smaller than in Field 04. This leads to a much greater shell thickness along the LOS. From Figures 5(d) and 7, the ionized shell in Fields 17 and 18 appears slightly more tenuous than in Field 04 (for roughly identical exposure times). This is not surprising since the particle density of the upstream neutral material is meant to decrease with latitude above the Galactic midplane (see Section 1). Considering larger line widths to be partially related to the accumulation of different radial velocity gradients along the LOS and itself highly favored in presence of dense erodible material (e.g., Flows L and N), the tenuous ionized material in Fields 17 and 18 could explain the particularly small values measured for $\langle\beta_{17,\mathrm{corr}}\rangle$ and $\langle\beta_{18,\mathrm{corr}}\rangle$ in Table 2.

The kinematical behavior of Flow S is best explained by the kinematics of the outer H I component found near the eastern boundaries of Fields 17 and 18 (see the interval of values for $v_{k,\mathrm{neutral}}$ presented for Flows T and U in Table 5). These radial velocities are roughly oriented along a "south-to-north" axis (between $b = 1.^\circ65$ and $b = 1.^\circ95$) toward a blueshifted tendency. Even though the value of -43 km s^{-1} does not particularly match $v_{S,\mathrm{initial}}$ (see Table 4), the ionized shell is likely to "follow" the kinematics of the atomic material.

Considering the 13 pc shell segment observed in Figure 7 as being density-bounded, the sustainment of each Hα filament, observed in the southern portion of Field 17, is likely provided

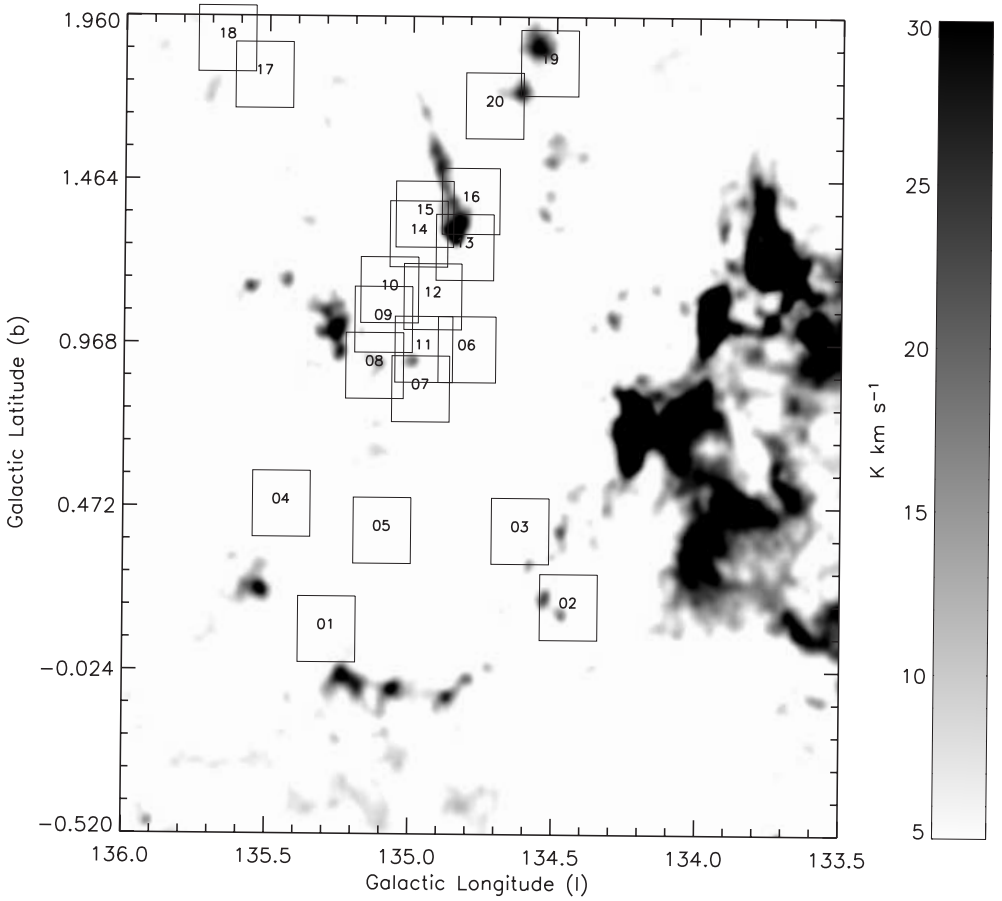

Figure 9. Integrated intensity map of the molecular emission found in the vicinity of the W4 region. The spectral collapse of the FCRAO CO (1–0) transition data cube was made for LSR radial velocities between −22.90 and −63.30 km s^{-1}. As in Figures 1 and 2, numbers coincide approximately with the location of the Fabry-Perot observations.

by IC 1805. The filamentary structures (at least, three of them are identified) have the same radial velocities as the thicker ionized shell and can be interpreted as observational evidences for a series of earlier shocks in a diffuse H I medium. Each of these shocks is likely to have contributed to the expansion of the large superbubble, the compressed H I now being fully ionized. This is in agreement with the multigeneration star cluster model postulated by Dennison et al. (1997) for the formation of W4 (see Section 2).

5.4. Interflow Medium

Before proceeding to the interpretation of the interflow medium, a quick return should be made on the eastern portion of Field 05, ignored in our definition of the interflow medium (see Section 4.4). A feature similar to the vertical ionized filament observed between the southern polar cap and Field 05 is seen emerging at roughly normal incidence from the dense western shell in the vicinity of Fields 02 and 03 (see Figure 2). The ionized filaments could correspond to dense fingers of shocked ISM material that have detached from the compressed shell (García-Segura et al. 1996; Capriotti & Kozminski 2001). Vishniac (1994) interpreted the streamers according to the theory of nonlinear thin shell instabilities where the shocked ISM material has a tendency to induce a momentum transfer directed in the opposite direction of the expansion. No particular radial velocity gradients are detected in the eastern portion of Field 05 and, therefore, suggest the ionized streamer to be observed perfectly parallel to the plane of the sky.

About the interflow medium, typical Galactic H II regions, in agreement with the Champagne model, present well-defined global radial velocity gradients encompassing the whole nebula. In Section 4.1, the range attributed to Flows A to X (see Table 4) was defined as the distance over which the radial velocity and line-width slopes for each flow remain roughly constant. Except for a few exceptions (e.g., Flows D, T, and U not associated with Champagne flows, Flow E limited by the FOV in Field 06, and Flow M voluntarily stopped in order to avoid overlap with the "slice-of-a-pie" regions of Flows L and N in Figure 6), this coincides, for a given flow, with the distance (on the plane of the sky) over which the ionized material has been carried away from its associated molecular feature. Compressive shocks are expected to be found at the end of these ranges (Shu et al. 2002). This can be seen from arched structures of compressed photoionized material beyond Flows G to K (see Figure 6) due to a large particle density of the ionized gas in the vicinity of the star cluster. W4-south, therefore, represents a very unique object since each detected Champagne flow expands in an interflow medium intrinsic to the superbubble and well defined kinematically (see the dotted histograms in Figures 3 and 4). In order to avoid a kinematical contamination from ionized flows that could have been omitted in Table 4, only the ionized material

Table 6
Transition Zones from the Intra to Interflow Medium

Beyond	Range	LSR Radial Velocities			Hα Line Widths		
		∇_v	$v_{\rm trans,initial}$	Correlation	∇_β	$\beta_{\rm trans,initial}$	Correlation
	(pc)	(km s^{-1} pc^{-1})	(km s^{-1})		(km s^{-1} pc^{-1})	(km s^{-1})	
Flow L	5.05	1.59 ± 0.07	−48.83 ± 0.26	0.95	−0.96 ± 0.04	15.68 ± 0.14	−0.96
Flow N	5.06	1.49 ± 0.15	−49.06 ± 0.56	0.95	−0.81 ± 0.05	15.53 ± 0.20	−0.96
Flow O	5.72	1.38 ± 0.09	−48.99 ± 0.39	0.97	0.12 ± 0.07	11.27 ± 0.29	0.62

observed in zones characterized by a low number of neutral features was considered in our investigation of the interflow medium. The star cluster vicinity was avoided since numerous cloud fragments are detected near $b = 0.^\circ9$ (see Figure 2). The value obtained for $\langle v_{\rm interflow,LSR}\rangle$ is redshifted by nearly 10 km s^{-1} with respect to $\langle v_{\rm FCRAO,CO}\rangle$ (see Section 5.1) and barely in agreement with the reddest end of the radial velocity range (between −38.46 and −45.05 km s^{-1}) revealing the H I cavity (see Section 2). Certainly, this interflow medium contributes to the 5 km s^{-1} gap between $\langle v_{\rm survey,LSR}\rangle$ and the mean radial velocity of the molecular material found in the vicinity of the W4 superbubble. The particularly low S/Ns measured for the interflow medium are easily explained from a lack of neutral and erodible material in the targeted regions.

Exceeding $\langle\beta_{\rm survey,corr}\rangle$ by roughly 2 km s^{-1}, $\langle\beta_{\rm interflow,corr}\rangle$ in Figure 4 indicates particularly broadened Hα profiles. This is expected from Fields 05, 12 and 20 since the ionized material is probed through deeper LOSs and, therefore, subject to an important kinematical disorder. However, the overabundance of radial velocities and line widths, respectively, above −35 km s^{-1} and 12 km s^{-1} in the dotted histogram of Figures 3 and 4 could be related to ionized material that results from the inner erosion of the H I supershell. In Section 5.3, this flowing "shell-to-interior" ionized material was characterized by particularly redshifted radial velocities (with respect to the neutral shell) and line broadening gradients directed toward the center of W4 (see Flows D, T, and U in Tables 4 and 5). The analogy used in Section 5.3 must consider the wake of lagging material to have a finite dimension. Once these gradients peaked (say, on a range of a few parsecs beyond the western boundaries of Fields 04, 17, and 18), the end radial velocities and line widths are likely to coincide with the right tails of the dotted distributions (therefore, partially explaining the kinematics of the interflow medium). Since shell segments entirely enclosing atomic material constitute a large fraction of the total shell's area, we anticipate the lagging ionized component to account for a large fraction of the interflow medium.

On a much smaller scale, the transition from the intra- to the interflow medium has been investigated. Since the extensions of Flows C and X are quickly limited by the FOV in Fields 03 and 20, respectively (see Figures 5(c) and 8), an investigation of the flows associated with the cloud fragment G134.6+1.9 is more appropriate. The mosaicked Hα peak intensity map of Figure 6 allows to quantify the gas's motion on ranges that exceed the dimensions of a single FOV. Panels (a) and (b) of Figure 10 present the kinematical behavior of the ionized material found beyond Flow L. The 6.25 pc range reaches the optical center of Field 12. The southern tip of the cloud fragment is located at 0 pc. Both panels have been splitted into three distinctive regions: (1) the (Champagne) Flow L followed by (2) a transition zone that finally leads to (3) the interflow medium. Well-defined tendencies are observed in regions (1) and (2). The linear fits are, respectively, represented by the bold and long-dashed lines (the bold lines correspond to the radial velocity and line-width gradients presented for Flow L in Table 4). Beyond region (3), no particular trend is observed in agreement with our expectations of a "chaotic" interflow medium. The abrupt change of the radial velocity slope between regions (1) and (2) could be a strong indication for a Champagne shock. Intuitively, region (2) of panel (a) looks very similar to the kinematical discontinuity, predicted between the upstream and downstream material of a shock (Shu 1992, Chapter 15). However, this discontinuity is expected to be only a few mean free paths thick, a fraction of a parsec. However, if we suppose the particle density at the boundary between regions (1) and (2) to be roughly equivalent to the mean density of the interflow medium in region (3), we could be confronted to a Champagne shock that has been almost fully dissipated.[2] Processes of diffusivity could be responsible for the return of ionized material in the upstream medium as the turbulent trapping becomes less and less efficient in the dissipating shock (Vainio & Laitinen 2007). The range of roughly 5 pc for region (2) in Figure 10 can be interpreted as the mixing length required for the escaping material to reach the local configuration of region (3). Beyond Flow L (in which end radial velocities are blueshifted with respect to the molecular material), the mixing length is characterized by a redshifted gradient estimated at 1.59 km s^{-1} pc^{-1}. The transition zone ends when the redshifted tendency vanishes near −41 km s^{-1}. The transition zone also shows a line narrowing gradient found at −0.96 km s^{-1} pc^{-1}. Even though the interflow medium was said to present particularly broadened Hα profiles (see above), the negative line-width gradient is explained by the efficiency of Flow L to induce line broadening. From end line widths near 15 km s^{-1} in Flow L, the transition zone ends with dispersion values slightly below 11 km s^{-1}, in agreement with $\langle\beta_{\rm interflow,corr}\rangle$.

Table 6 presents similar investigations made for Flows N and O along the western edge of G134.9+1.4. The transition zone of Flow N is very similar to region (2) in Figure 10, presenting identical mixing lengths and similar gradients. However, the change in the angle of view from Flow L (and N) to Flow O has a sizeable impact not only on the kinematics of the Champagne flow (see Section 5.2) but also on the transition zone. For a mixing length that slightly exceeds the transition zones beyond Flows L and N, a flatter radial velocity gradient is obtained beyond Flow O that also leads to radial velocities near −40 km s^{-1}. In Table 6, the small value extracted for ∇_β is mostly associated with end line widths for Flow O already in agreement with the interflow medium (see Table 4). The transition zone is, therefore, barely distinguishable if we limit ourselves to the line-width behavior beyond Flow O.

Flows I and J present extensions that approximately lead to the optical center of Field 12, in the vicinity of the extended

[2] An exponential decrease of the flow's particle density is predicted from the Champagne model as the photoionized material is carried away from the eroded neutral feature (Tenorio-Tagle 1979; Bodenheimer et al. 1979).

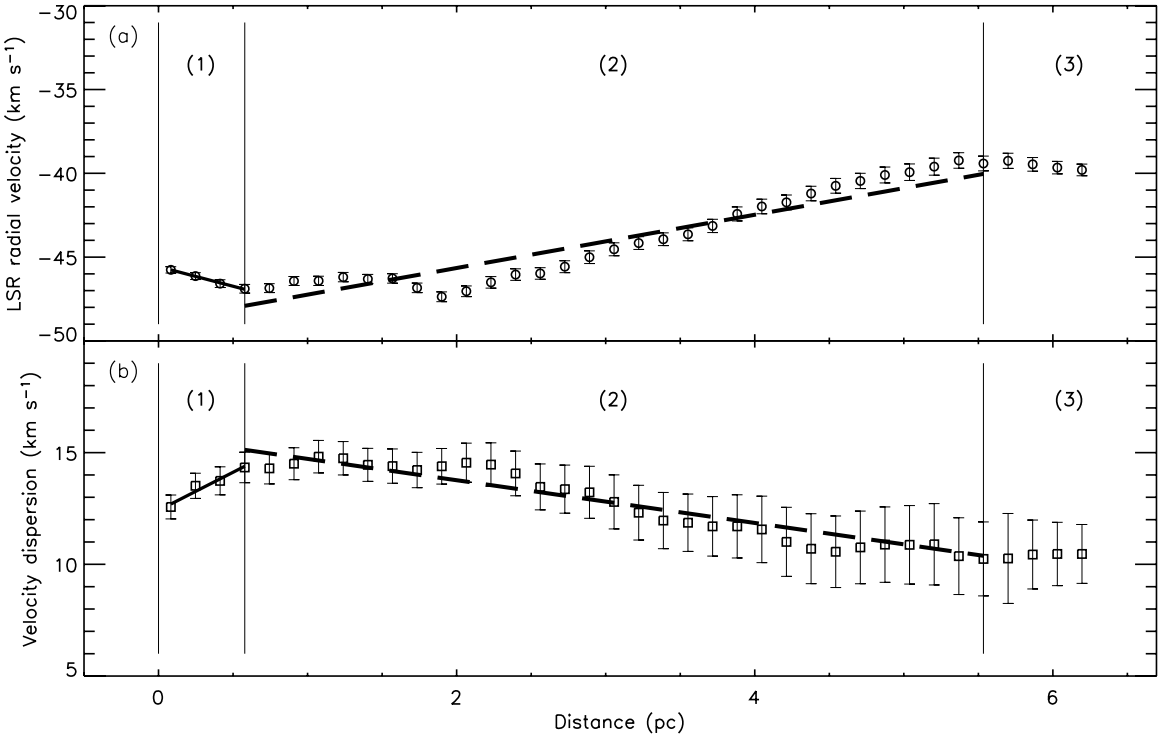

Figure 10. Kinematical behavior of the ionized material in and slightly beyond Flow L. Panels (a) and (b), respectively, correspond to the radial velocity and Hα line-width profiles. The cloud fragment G134.9+1.4 is located at 0 pc. Three regions are defined: (1) the Champagne Flow L followed by (2) the transition zone that leads to (3) the interflow medium. The linear fits associated with regions (1) and (2) correspond, respectively, to the bold and long-dashed lines.

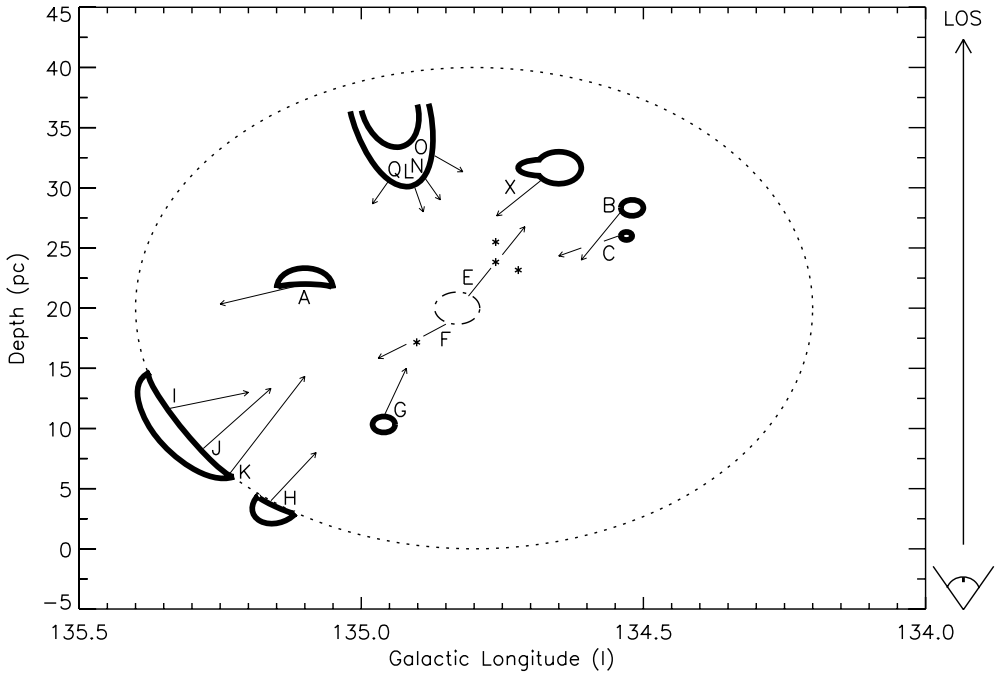

Figure 11. Longitudinal cut, as seen from above, of the W4 superbubble between $b = 0.^{\circ}0$ and $b = 1.^{\circ}8$. The dotted line is related to the semineutral, semi-ionized supershell. The molecular cloud fragments correspond to the thick solid lines. The central Hα feature in Field 06 is represented by the dash-dotted line since its molecular counterpart is hardly distinguishable from the FCRAO (1–0) observations. The approximate direction of each flow is shown by solid arrows. The "*" symbols coincide with the four O stars in Figure 6. The observer is located "below" the figure.

Flow L of Figure 10 (a priori, these two flows are not kinematically contaminated by other accelerated flows in the vicinity of the star cluster). The radial velocity and line-width profiles, beyond both flows, present plateaux intersected by a small range (< 1 pc) of decreasing/increasing trends, a behavior we would anticipate from the interflow medium. The arched structures of compressed ionized material in Figure 6 indicate a particle density that likely exceeds the shock's density of Flows L, N, and O. The mixing length beyond Flows I and J might, therefore, be very restricted or even null if we suppose no ionized material to escape from the compressive shocks.

6. SPATIAL SCENARIO

The interpretation of the radial velocity behavior of particular flows presented in Table 4 allows a three-dimensional representation of the molecular fragments found embedded or at the periphery of W4-south. A longitudinal cut of W4 in the latitude range between $b = 0.^{\circ}0$ and $b = 1.^{\circ}8$ is presented in Figure 11 (seen from above the Galactic plane). The dotted line represents the semineutral, semi-ionized supershell at the latitude of the star cluster, assuming a roughly elliptical shape (estimated from the distance separating the western and the eastern walls in Figure 2). Obviously, the size (or "depth" according to Figure 11) of the ellipse is meant to vary with latitude (practically null at $b = 0.^{\circ}0$ to roughly 60 pc near $b = 1.^{\circ}8$). From the 13 OB stars shown in Figure 6, only four O stars were drawn in Figure 11. The location of each star and cloud fragment remains approximate but probably not too far from reality. Each flow is identified by the same letter as in Table 4. The angle of each flow with respect to the LOS is estimated from the ∇_v values in Table 4 and the maximal value expected from a Champagne flow. The solid arrows indicate the most plausible directions. The flatter gradients (e.g., A, C and I) generally indicate molecular material roughly coplanar with the photon flux orientation and, therefore, Champagne flows roughly perpendicular to the LOS. Inversely, steeper gradients (e.g., K, L, and N) are related to Champagne flows presenting an important velocity component parallel to the LOS and, therefore, propose the associated molecular fragments to be located either in front or behind the ionizing sources. Flows M and R were voluntarily omitted in order to avoid confusion in Figure 11.

7. CONCLUSION

The use of an interferometric device system, especially designed to study particularly faint extended astronomical objects, has allowed us to extract the kinematical information associated with the ionized component found embedded in the southern portion of the Galactic superbubble/H II region W4. Prior to our investigation, the superbubble was presented as a promising candidate of Galactic chimney likely to energetically interact with the Galactic corona. From 20 Hα data cubes, the photoionization of numerous molecular clumps, found embedded or compressed along the expanding outer shell, leads to the detection of at least 10 independent flows of eroded ionized material in agreement with the Champagne model for the time-dynamical evolution of H II regions (Flows L to R, e.g, were interpreted as a unique flow since they all involve a single cloud fragment). Radial velocity gradients between 0.31 and 2.60 km s^{-1} pc^{-1} (in absolute value) are detected (Section 4.2). The steepness of each radial velocity gradient approximately indicates the angle of the ionized flow with respect to the LOS and, therefore, the position of the eroded material with respect to the ionizing sources. A spatial scenario is proposed for the distribution, along the LOS, of each investigated cloud fragment in W4-south (Section 6). Clearly, W4-south shows the last stage of the photoerosion of a large giant molecular cloud. At the periphery of the expanding bubble, cloud fragments, located above (below) the star cluster, present associated Champagne flows redshifted (blueshifted) with respect to the molecular material (Section 5.2). This is in agreement with the W4 superbubble being tilted toward the observer.

The radial velocity gradients all present slopes smaller than the maximal gradient expected from the Champagne phase (between 3 and 5 km s^{-1} pc^{-1}). Gas flows generally perpendicular to the LOS are proposed in order to explain the low kinematical disorder observed on the plane of the sky (Section 5.1). A kinematical contribution to the observed gradients attributed to stellar winds could not be verified and could be related to this geometrical effect (Section 5.2). However, stellar winds might also have a negligible contribution to the kinematics of the ionized material embedded in well-developed flows near the star cluster (Section 5.2).

The particle density contrast at the pressure discontinuity between the erodible neutral material and the surrounding ISM also presents sizeable repercussions on the observed kinematics. In particular, the inner erosion of the W4 supershell, formed of either partially compressed molecular clumps or atomic material, reveals many different mechanisms. In the first case, accelerated (blueshifted or redshifted) flows in agreement with the Champagne model are observed as expected (Section 5.2). The photoerosion of the atomic shell, characterized by a local particle density roughly 3 to 10 times smaller than the minimal density expected on the outer envelope of molecular clouds, induces redshifted (with respect to the neutral H I shell) flows directed toward the center of the expanding bubble. Rather than being interpreted as backward Champagne flows, the eroded material is said to "hover," left behind the advancing (toward the observer) supershell. The kinematics of these particular flows has been largely compared to a wake of material behind a solid body moving in a viscous fluid (Section 5.3). This lagging material could have a sizeable impact on the kinematics of some restricted zones of our Hα survey of W4-south referred to as the interflow medium (Section 5.4).

Particular Champagne shocks present evidences of shock dissipation. The transition from the intra- to interflow medium shows a mixing length in which accelerated ionized material escapes the compressive shock and gradually evolves to recover the local kinematical state of the interflow medium (Section 5.4). The interflow medium partially explains the overall mean radial velocity of our Hα survey to be redshifted by roughly 5 km s^{-1} from the mean radial velocity of the molecular material observed in the vicinity of the W4 complex (Sections 5.1 and 5.4).

The investigation of the kinematical disorder along the LOS shows W4 to lie in a transient state between subsonic and supersonic regimes, in agreement with the apparent dimensions of the superbubble. The mean Hα line width is estimated at 9.213 ± 0.002 km s^{-1}. W4-type superbubbles, characterized by complicated radial velocity fields, are assumed to be the missing link between small-size (< 30 pc) Galactic and giant (> 500 pc) extragalactic H II regions (Section 5.1). The Hα linewidth behavior, intrinsic to Champagne flows, is particularly investigated. Tendencies toward line broadening, in agreement with the theory, are mostly explained by a series of effects; the constant increase of the investigated volume of ionized material along the LOS, the addition of radial velocity gradients as the eroded material is carried away from the pressure discontinuities (between the molecular and interstellar material), a localized spreading of the ionizing sources in the vicinity of the erodible material, and porosity and imperfections on the outskirts of the neutral clumps (Section 5.2). The line broadening gradients for Champagne flows are found between 0.16 and 3.62 km s^{-1} pc^{-1} (Section 4.2). However, line narrowing gradients, in the vicinity of the star cluster, are attributed to absorption along the LOS, thus blocking a certain fraction of the kinematical information (Section 5.2).

The ionized material found embedded in W4-south being mostly dominated by small-scale ($\lesssim$ 10 pc) Champagne flows, no large-scale gas flows are detected (Section 5.1). This is in disagreement with the model of Galactic chimney (Section 1). From the imposing distance ($\sim$ 180 pc) on the plane of the sky separating the northernmost portion of the superbubble and W4-south, we propose large-scale ionized flows to remain undetected below a certain threshold in latitude. In order to estimate the implication of the W4 superbubble in the sustainment of the Galactic corona, a similar investigation, carried out through Fabry-Perot interferometry in Paper II, will provide information on the kinematics and dynamics related to the ionized material found embedded in W4-north.

The authors thank the Natural Sciences and Engineering Research Council of Canada and the Fonds Québécois de la Recherche sur la Nature et les Technologies who provided funds for this research project. The Canadian Galactic Plane Survey is a Canadian project with international partners and is supported by a grant from the Natural Sciences and Engineering Research Council of Canada. Data from the Canadian Galactic Plane Survey are publicly available through the facilities of the Canadian Astronomy Data Centre (http://www1.cadc-ccda.hia-iha.nrc-cnrc.gc.ca/cgps/).

D.L. is grateful to M.-A. Miville-Deschênes and Olivier Daigle who provided useful IDL routines to carry out data reduction. D.L. also thanks B. Malenfant, G. Turcotte, and P.-L. Lévesque for technical support during numerous observing nights at the Observatoire du mont Mégantic. Finally, D.L. thanks astro-imager R. Crisp for providing the Light from the Heart.

REFERENCES

Atherton, P. D., Taylor, K., Pike, C. D., Harmer, C. F. W., Parker, N. M., & Hook, R. N. 1982, MNRAS, 201, 661
Barriault, L., & Joncas, G. 2007, ApJ, 667, 257
Basu, S., Johnstone, D., & Martin, P. G. 1999, ApJ, 516, 843
Bevington, P. R. 1969, Data Reduction and Error Analysis for the Physical Sciences (New York: McGraw-Hill)
Blitz, L., Fich, M., & Stark, A. A. 1982, ApJS, 49, 183
Bodenheimer, P., Tenorio-Tagle, G., & Yorke, H. W. 1979, ApJ, 233, 85
Callaway, M. B., Savage, B. D., Benjamin, R. A., Haffner, L. M., & Tufte, S. L. 2000, ApJ, 532, 943
Capriotti, E. R., & Kozminski, J. F. 2001, PASP, 113, 677
Chevalier, R. A., & Gardner, J. 1974, ApJ, 192, 457
Comerón, F. 1997, A&A, 326, 1195
Cyganowski, C. J., Reid, M. J., Fish, V. L., & Ho, P. T. P. 2003, ApJ, 596, 344
Daigle, O., Carignan, C., Hernandez, O., Chemin, L., & Amram, P. 2006, MNRAS, 368, 1016
Dennison, B., Topasna, G. A., & Simonetti, J. H. 1997, ApJ, 474, 31
Dickey, J. M., & Lockman, F. J. 1990, ARA&A, 28, 215
Digel, S. W., Lyder, D. A., Philbrick, A. J., Puche, D., & Thaddeus, P. 1996, ApJ, 458, 561
Dyson, J. E., & Meaburn, J. 1971, A&A, 12, 219
Felli, M., Habing, H. J., & Israël, F. P. 1977, A&A, 59, 43
Field, G. B., Goldsmith, D. W., & Habing, H. J. 1969, ApJ, 155, 149
Franco, J., Tenorio-Tagle, G., & Bodenheimer, P. 1990, ApJ, 349, 126
Gach, J.-L., et al. 2002, PASP, 114, 1043
García-Segura, G., Mac Low, M.-M., & Langer, N. 1996, A&A, 305, 229
Godbout, S., Joncas, G., & Drissen, L. 1998, PASA, 15, 60
Godbout, S., Joncas, G., Durand, D., & Arsenault, R. 1997, ApJ, 478, 271
Heiles, C. 1991, IAUS, 147, 43
Henney, W. J., Arthur, S. J., & Garciá-Díaz, Ma. T. 2005, ApJ, 627, 813
Henny, J. G., Lamers, L. M., & Cassinelli, J. P. 1999, Introduction to Stellar Winds (Cambridge: Cambridge Univ. Press)
Hernandez, O., Gach, J.-L., Carignan, C., & Boulesteix, J. 2003, Proc. SPIE, 4841, 1472
Hester, J. J., et al. 1996, AJ, 111, 2349
Heyer, M. H., Brunt, C., Snell, R. L., Howe, J. E., & Schloerb, F. P. 1998, ApJS, 115, 241
Hippelein, H., & Fried, J. W. 1984, A&A, 141, 49
Jenkins, E. B., & Meloy, D. A. 1974, ApJ, 193, 121
Joncas, G., & Roy, J.-R. 1984, ApJ, 283, 640
Joncas, G., & Roy, J.-R. 1986, ApJ, 307, 649
Kutner, M. L. 1984, Fundam. Cosm. Phys., 9, 233
Lagrois, D., & Joncas, G. 2009, ApJ, in press (Paper II)
Landau, L. D., & Lifshitz, E. M. 1987, in Fluid Mechanics (2nd ed.; Toronto: Permagon Press)
Lee, Y., et al. 1999, ApJS, 138, 187
Lenz, D. D., & Ayres, T. R. 1992, PASP, 104, 1104
Llorente de Andrés, F., Burki, G., & Ruiz del Arbol, J. A. 1982, A&A, 107, 43
Massey, P., Johnson, K. E., & DeGioia-Eastwood, K. 1995, ApJ, 454, 151
McClure-Griffiths, N. M., Dickey, J. M., Gaensler, B. M., Green, A. J., Haynes, R. F., & Wieringa, M. H. 2000, AJ, 119, 2828
McClure-Griffiths, N. M., Ford, A., Pisano, D. J., Gibson, B. K., Staveley-Smith, L., Calabretta, M. R., Dedes, L., & Kalberla, P. M. W. 2006, ApJ, 638, 196
McClure-Griffiths, N. M., Green, A. J., Dickey, J. M., Gaensler, B. M., & Wieringa, M. H. 2001, ApJ, 551, 394
McKee, C. F., & Ostriker, J. P. 1977, ApJ, 218, 148
Miville-Deschênes, M.-A., Joncas, G., & Durand, D. 1995, ApJ, 454, 316
Müller, P., Reif, K., & Reich, W. 1987, A&A, 183, 327
Norman, C. A., & Ikeuchi, S. 1989, ApJ, 345, 372
Normandeau, M., Taylor, A. R., & Dewdney, P. E. 1996, Nature, 380, 687
Normandeau, M., Taylor, A. R., & Dewdney, P. E. 1997, ApJS, 108, 279
O'Dell, C. R., & Townsley, L. K. 1988, A&A, 198, 283
Osterbrock, D. E., Fulbright, J. P., Martel, A. R., Keane, M. J., Trager, S. C., & Basri, G. 1996, PASP, 108, 277
Paladini, R., Davies, R. D., & DeZotti, G. 2004, MNRAS, 347, 237
Rosa, M., & Solf, J. 1984, A&A, 130, 29
Sáinz, A., García, M. C., & Calzada, M. D. 2005, in 32nd EPS Conference on Plasma Physics 29C, ed. C. Hidalgo & B. Ph. van Milligen (Bristol: IOP Publishing), 4.132
Shi, H. M., & Hu, J. Y. 1999, A&AS, 136, 313
Shu, F. H. 1992, Gas Dynamics, Vol. 2 (Mill Valley, CA: Univ. Science Books)
Shu, F. H., Lizano, S., Galli, D., Cantó, J., & Laughlin, G. 2002, ApJ, 580, 969
Spitzer, L. Jr 1956, ApJ, 124, 20
Taylor, A. R., Irwin, J. A., Matthews, H. E., & Heyer, M. H. 1999, ApJ, 513, 339
Tenorio-Tagle, G. 1979, A&A, 71, 59
Tenorio-Tagle, G., & Bedjin, J. P. 1981, A&A, 99, 305
Tenorio-Tagle, G., Beltrametti, M., Bodenheimer, P., & Yorke, H. W. 1982, A&A, 112, 104
Terebey, S., Fich, M., Taylor, R., Cao, Y., & Hancock, T. 2003, ApJ, 590, 906
Vainio, R., & Laitinen, T. 2007, ApJ, 658, 622
Vishniac, E. T. 1994, ApJ, 428, 186
Wang, X., & Dalton, C. 1991, Int. J. Numer. Methods Fluids, 12, 383
Watson, C., Zweibel, E. G., Heitsch, F., & Churchwell, E. 2004, ApJ, 608, 274
West, J. L. 2003, Master Thesis, Univ. of Manitoba, Canada
West, J. L., English, J., Normandeau, M., & Landecker, T. L. 2007, ApJ, 656, 914
Westerhout, G. 1958, Bull. Astron. Inst. Neth., 14, 215
Yentis, D. J., Novick, R., & van den Bout, P. 1972, ApJ, 177, 375
Yorke, H. W., Tenorio-Tagle, G., & Bodenheimer, P. 1984, A&A, 138, 325